Fatigue crack growth of butt welded joints subjected to mixed mode loading and overloading

Shakeri, Iman; Shahani, Amir Reza; Rans, Calvin David

DOI
10.1016/j.engfracmech.2020.107376

Publication date
2021

Document Version
Accepted author manuscript

Published in
Engineering Fracture Mechanics

Citation (APA)
Shakeri, I., Shahani, A. R., & Rans, C. D. (2021). Fatigue crack growth of butt welded joints subjected to mixed mode loading and overloading. *Engineering Fracture Mechanics*, *241*, Article 107376. https://doi.org/10.1016/j.engfracmech.2020.107376

Fatigue crack growth of butt welded joints subjected to mixed mode loading and overloading

Iman Shakeri [a], Amir Reza Shahani [b,*], Calvin David Rans [c]

[a] Fracture Mechanics Research Laboratory, Department of Applied Mechanics, K.N. Toosi University of Technology, Tehran, Iran.

E-mail address: iman.shakeri1368@gmail.com

[b,*] Corresponding author. Faculty of Mechanical Engineering, Department of Applied Mechanics, K.N. Toosi University of Technology, P.O. Box 19395-1999, Tehran, Iran. Tel.: +98 21 84063221; Fax: +98 21 88677273.

E-mail address: Shahani@kntu.ac.ir

[c] Faculty of Aerospace Engineering, Delft University of Technology, Kluyverweg 1, 2629 HS Delft, The Netherlands.

E-mail address: c.d.rans@tudelft.nl

Abstract

In this paper, fatigue crack growth behavior of Al5083 welded joint under mixed mode loading was firstly studied. Afterwards, fatigue crack growth behavior of butt welded joints under a mixed mode overload has been investigated. Influence of post weld heat treatment on retardation caused by overload was also studied. It was shown that two existing retardation models for non-welded material subjected to mixed mode overload are not capable to predict retardation of welded joints accurately. By including the effect of residual stress to the models, an extension to them was proposed to enhance the accuracy of them for welded joints.

Keywords: Mixed mode loading; Fatigue crack growth; overload; retardation; residual stress.

Nomenclature

a	Crack length
a_d	Delay length or retarded crack length
a_{ol}	Crack length at which the overload is applied
C	Paris constant
C_p^*	Mixed mode retardation parameter
E	Modulus of elasticity
F	Uniaxial applied load
F_{max}^{Bl}	Maximum applied load
F_{min}^{Bl}	Minimum applied load
F^{ol}	Applied overload
$h_{\text{convection}}$	Convection coefficient
h_{total}	Total heat loss coefficient
I	Arc current
K_{max}^{Bl}	Maximum stress intensity factor of baseline
K_I^d	Maximum stress intensity factor at a_d
K_{eq}	Equivalent stress intensity factor
K_{I}	Stress intensity factor of mode I
$K_{\text{I,applied}}$	Applied stress intensity factor
$K_{\text{I,eff}}$	Effective stress intensity factor
K_{II}	Stress intensity factor of mode II
K_{eq}^{ol}	Equivalent stress intensity factor for applied overload
K_{Res}	Residual stress intensity factor
m_I	Wheeler exponent
m^*	Mixed mode exponent
N	Cycle
N_d	Delay cycles
n	Paris constant
q	Heat flux
$q_{\text{convection}}$	Heat loss through convection
$q_{\text{radiation}}$	Heat loss through radiation

Q	Heat input
r	The area in which the heat flux is acted
r_b	The area in which 95% of the heat flux is deposited
r_p	Plastic zone size
$r_{p,d}$	Plastic zone size at K_I^d
$r_{p,ol}$	Overload plastic zone size at a_{ol}
R	Loading ratio
R^{Bl}	Baseline loading ratio
R^{ol}	Overload ratio
S_{22}	Transverse component of stress
S_y	Yield Strength
t	Time
T	Temperature
T_a	Ambient temperature
T_i	Current temperature
v	Welding speed
V	Arc voltage
w	Specimen width
x_h	Location of center point of moving heat source
α	Plastic zone size factor
β	Loading angle
ΔK	Stress intensity factor range
ΔK_{eq}	Equivalent stress intensity factor range
$\Delta K_{\mathrm{eq,eff}}$	Equivalent effective stress intensity factor range
$\Delta K_{\mathrm{I,eff}}$	Effective stress intensity factor range
$\varepsilon_{\mathrm{em}}$	Emissivity
η	Arc efficiency
σ_{bol}	Stefan-Boltzman constant

1. Introduction

Al-Mg alloy of 5xxx series is widely used in the marine, pressure vessel and aerospace industries due to its excellent weldability, corrosion resistance and high toughness [1]. It is well-known that fatigue loading is the main cause of failure in these industries. In many practical cases the loading direction as well as loading amplitude may change. Also, the weld zone in structures are the most critical area for crack initiation. So, special attention to welded joints under different loading conditions is required.

Kim [2] examined fatigue behavior of the crack at the weld root subjected to mixed mode I and III loading and it was shown that the fatigue crack growth life of the specimens can be estimated with almost the same accuracy by employing the equivalent stress intensity factor range. Zhu et al. [3] investigated fatigue crack growth in the heat affected zone (HAZ) of a butt welded specimen subjected to mixed mode loading conditions. They observed that the FCGR was decreased by increasing in mode II portion of fatigue loading. Creating inclined crack, the influence of strain strengthening on crack growth rate and path under mixed mode loading conditions has been investigated by Tang et al. [4]. They stated that the crack changes its direction from mixed mode to mode I. Also, it was observed that strain strengthening has influence on the crack growth rate, while it has no influence on the crack growth paths. Jie et al. [5] studied growth behavior of fatigue crack in fillet cruciform welded joints with 45° inclination angle in which mixed mode stress field appear at the weld toe and then, results of numerical simulation were compared to the experimental results. However, welding residual stress was not considered in their work.

Until now, little research has focused on the effect of welding residual stress on fatigue crack growth behavior of welded joints subjected to mixed mode loading. Ma et al. [6] investigated fatigue crack growth of welded joints subjected to mixed mode loading. In their experiments, the crack was created at the weld toe and it was parallel to the welding direction. Their experimental results showed that the fatigue crack growth rate (FCGR) of welded specimen is less than that of base non-welded specimen and they proposed a model on the basis of the initial distribution of

residual stress. However, redistribution of residual stress was not considered. Wang et al. [7] studied mixed mode fatigue crack growth of welded joint in high strength steel. They did not used as-weld specimen and some mechanical operations and post weld heat treatment was conducted on weldment. It was shown that due to the compressive welding residual stress in the longitudinal direction, the crack opening force in pure mode I is lower than that in mixed mode loading in which the low level of crack closure is caused by the compressive welding residual stress in the transverse direction. Based on experimental results, they proposed an equivalent stress intensity factor to correlate fatigue crack growth data.

Overload is another important parameter which has an influence on the FCGR [8] and is defined as large stress peak in an otherwise constant amplitude load history. Applying the overload, a large amount of plastic deformation around the crack tip is created. Due to the interaction between plastic and elastic areas, the residual compressive stress field appears around the crack tip and consequently the fatigue crack growth is retarded [9]. Several models have been proposed for calculating retardation caused by overload [10,11]. Among them, Wheeler retardation model [12] is one of the most practical models. Many modifications to Wheeler model have been proposed by investigators [13-16]. However, these models are restricted to pure mode I overload conditions.

The problem becomes more complicated if mixed mode conditions prevail at the crack tip by changing in the overload direction due to a special event such as thermo-shock or an operating error or temporary change in the loading direction [11]. For this purpose, some studies have focused on the fatigue crack growth behavior of materials subjected to mixed mode overload [17-24]. Sander and Richard [17] numerically showed that an increase in mode II portion of the overload causes a decrease in crack closure. Results of mixed mode overload experiments showed that the largest retardation occurred in the case of pure mode I overload and as the portion of mode II overload increases, the amount of retardation decreases [18,19]. Using the multi-focused optical microscope, Lee and Choi [20] noticed that as the shear portion of overload increases, the fatigue crack tip is sharpened and also the damage zone in the vicinity of the crack front is rotated. By conducting

several experiments on cruciform geometry specimens, Datta et al. [21] observed that the retardation caused by overload is proportional to the crack length and magnitude of overload, while no monotonic behavior was observed between the increase in the fatigue life and the value of mode mixity. It was shown that the fatigue crack growth rate is more consistent with change in the value of mode mixity and also the retardation of crack growth is continuously decreased by increasing in the value of mode mixity [22].

By applying mixed mode overload to tubular specimens, Rege et al. [23] showed that retardation length is more than two times longer than the size of the overload plastic zone obtained from a linear elastic solution. Shahani et .al [24] proposed two models to evaluate retardation of fatigue crack growth of non-welded specimen under mixed mode overload by extending the Wheeler retardation model. In their first model, retardation can be predicted with high accuracy. However, their second model can be more practical since it does not include more material constants than the Wheeler model. All the aforementioned models have been proposed for non-welded structures and their application to the welded joints has not been examined. As a result of plastic strains caused by local heating and cooling during the welding process, residual stress takes place affecting the fatigue crack growth of welded joints [25] and it should be taken into account in retardation models.

In the first step of the present research, the effect of mixed mode fatigue loading on the crack growth behavior of Al5083 welded and non-welded specimens is investigated. It is shown that the fatigue crack growth rate of welded joints can be correlated with that of non-welded specimens at the same loading conditions by including the effect of residual stress caused by welding. In the second stage, the effect of mixed mode single overload on the fatigue crack propagation of welded specimens is investigated. In this case, the baseline fatigue loading prior to and after overload, was applied under pure mode I and only single overload was applied under mixed mode conditions. In the meanwhile, effect of post weld heat treatment (PWHT) on retardation of fatigue crack growth for pure mode I overload is examined and it is shown that it leads to a significant reduction in

retardation. By including residual stress effect into the two previous retardation models proposed for non-welded specimens, an extension of them is provided to enhance the accuracy of the models for welded joints under mixed mode overload.

2. Experiments

2.1. Material specification

The material employed in this research was 5083-H111 aluminum alloy with thickness of 5 mm. The chemical composition of aluminum alloy 5083-H111 is presented in Table 1.

Table 1. Chemical composition (wt.%) of base metal and weld metal.

Element	Si	Fe	Cu	Mn	Mg	Zn	Ti	Cr	Al
Base Meatal (AA5083)	0.4	0.4	0.1	0.75	4.45	0.25	0.15	0.15	bal
Weld metal (AA5183)	0.4	0.4	0.1	0.75	4.75	0.25	0.15	0.15	bal

Prior to the welding process, welding parts were wiped with ethanol in order to remove the impurities of the surfaces and a wire brush was employed to eliminate the aluminum oxide. Fig. 1 shows the Single ‘V’ butt joint configuration. The welding of the sheets was performed using TIG (Tungsten Inert Gas) welding process, with AA5183 used as the filler metal. The chemical composition of the filler metal is given in Table 1. The sheets were welded in a single pass and during the welding process, temporary stainless steel backing bar, as shown in Fig. 1, was used to support and shield molten weld metal. The direction of welding was parallel to the rolling direction. In order to avoid joint distortion the sheets were fixed with suitable clamps during the welding process.

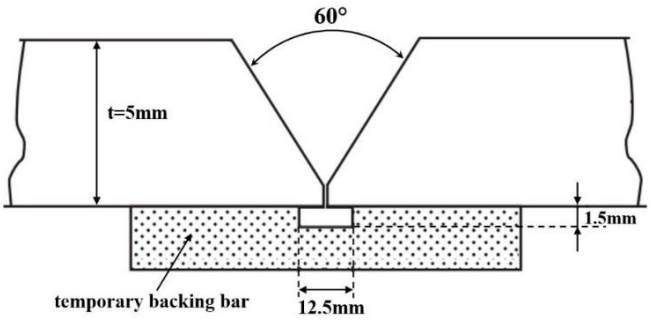

Fig 1. Joint configuration.

The welding parameters applied for TIG welding are presented in Table 2.

Table 2. Welding process parameters

Parameter	Values
Current	210 A
Voltage	10 v
Filler rod diameter	4 mm
Tungsten electrode diameter	3 mm
Welding speed	3 mm/s
Shielding gas	Argon
Gas flow rate	12 lit/min

Preparing tension test specimens from both base metal and the welded joint, tensile experiments were performed. Table 3 shows the mechanical properties of the base metal and welded joint at the ambient temperature.

Table 3. Mechanical properties of the base metal and welded joints at ambient temperature.

	E (GPa)	Poisson's ratio	0.2% Proof Stress (MPa)	Tensile Strength (MPa)	Elongation (%)
Base metal	65±0.8	0.33	140±1.5	309±4	22.1±0.6
Welded joint	60±0.5	0.33	127±1	263±1.6	10.3±0.1

2.2. Experimental Procedure

Mixed mode (mode I and mode II) fatigue crack growth experiments were carried out on both weld metal and base metal using Compact Tension Shear (CTS) specimen introduced by Richard and Benitz [26]. Fig. 2 illustrates geometry of the CTS specimen employed in the present investigation including relevant details regarding the mixed mode fixture.

(a)

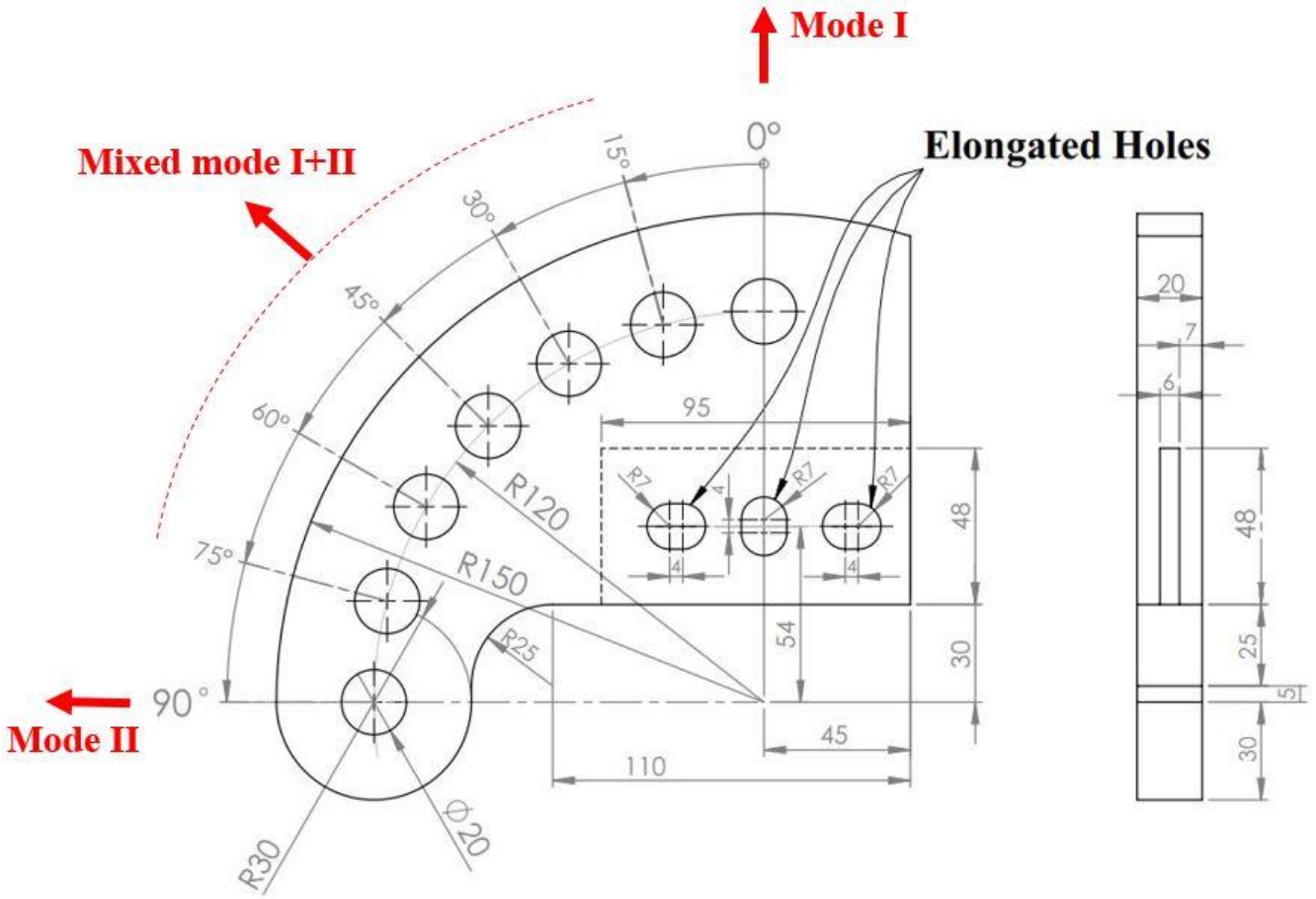

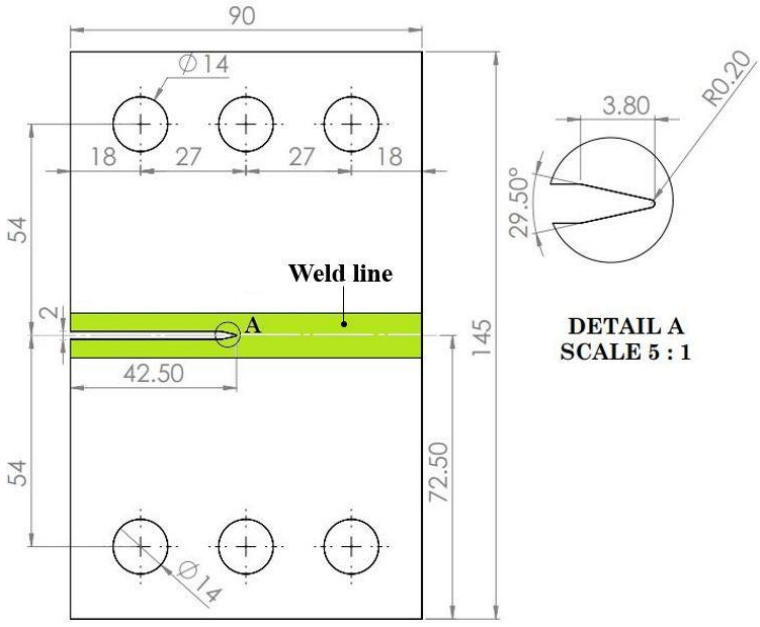

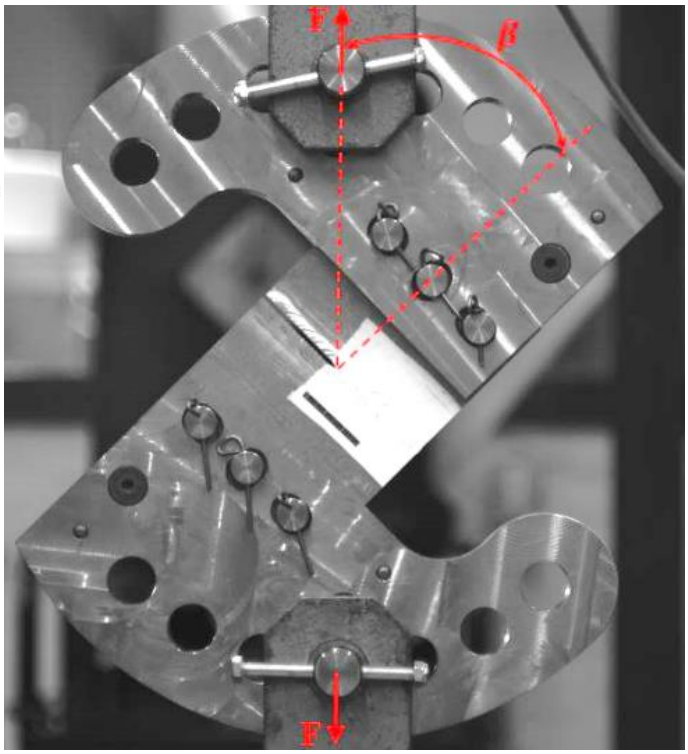

(b) (c)

Fig. 2. Drawing of the (a) fixture and (b) CTS specimen, dimensions are in mm. (c) mixed mode fixture.

Initial notch was created by electro-discharge machining at the center of the weld line. The direction of initial notch is parallel to the welding direction in welded specimen (WM) and is

parallel to the rolling direction in base metal specimen (BM). The designed fixture was made from 17-4 PH stainless steel and its dimensions were obtained by analyzing the fixture using ABAQUS 6.14 [27] in such a manner that the stresses were lower than the endurance limit of the aforementioned steel.

Different mixed mode loading conditions can be created at the crack tip by rotating the specimen and the fixture with various angles β. As illustrated in Fig. 2, it can be assured that the loads are transmitted from the fixture to the CTS specimen in the horizontal and vertical directions by making elongated holes on the fixture.

The tests were performed employing an MTS 60 kN servo-hydraulic fatigue machine. All the experiments were conducted at ambient temperature with the loading ratio $R(= F_{min}/F_{max})$ of 0.1 and frequency of 20 Hz.

The test specimens were fatigue precracked under pure mode I loading conditions up to $a_{front}/w = 0.555$, where a_{front} and w are the crack length at the front side and width of the specimen, respectively.

Two groups of experiments were conducted. Fig. 3 shows the loading pattern of these two groups. In the first group (i.e. mixed mode constant amplitude loading experiments) presented in Section 3, after the fatigue precracks were created, the specimens were tested under constant amplitude loading at $\beta = 0,15,30,45^{\circ}$ with respect to the axis perpendicular to the crack plane (Fig. 3a).

In the second group (i.e. mixed mode overload experiments) presented in Section 4, only the single overload was applied under mixed mode conditions and the baseline fatigue loading prior to and after applying overload, was applied under pure mode I conditions (Fig. 3b). For this purpose, after fatigue precracking, to create mixed mode conditions the loading angle was changed to four various mode mixities of $\beta = 0,15,45,90^{\circ}$ by rotating the fixture. Then, the specimens were subjected to single overload spike at a loading rate of 0.2 kN/s. Thereafter, by returning the fixture to $\beta = 0^{\circ}$, fatigue loading was continued under pure mode I conditions the same as loading prior to

overload. In order to investigate the effect of post weld heat treatment on the retardation caused by overload, a welded specimen was subjected to heat treatment. For this purpose, a welded specimen was kept at 250°C for 1 hour and then cooled to ambient temperature in a heat chamber.

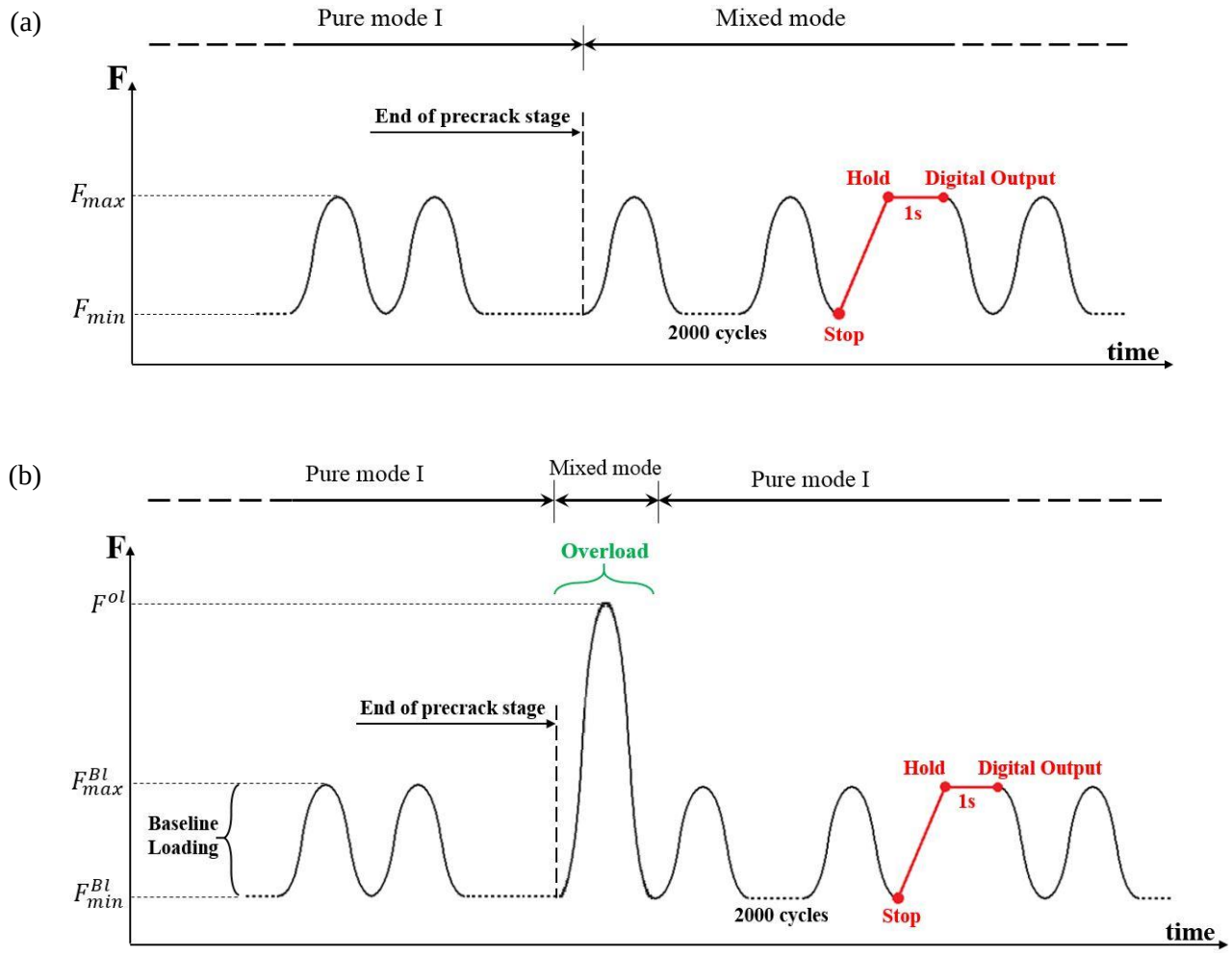

Fig. 3. Schematic of loading pattern for (a) group I: mixed mode constant amplitude loading experiments (b) group II: mixed mode single overload experiments.

The crack length of the specimen was measured by visual method. For the welded joint, the crack length measurement was performed on both sides of the specimen. During crack growth, digital images of the crack tip region were recorded using two cameras with resolution of 2448 by 2048. In order to enhance optical capability of the crack length measurement, the region ahead of the crack tip was painted with white color. For more accurate detection of the crack tip, the photos were taken when the cracks was completely open. As shown in Fig. 3, fatigue loading was stopped

at the minimum load every 2000 cycles and then the load was increased to 95% of the maximum load and held for 1 second and after that signals were sent to the cameras to take pictures.

Due to the asymmetric geometry of the weld, the crack length on the two sides of the specimen varies widely. Fig. 4 shows the comparison between the measured crack length during the test by digital cameras and the actual crack length at the end of the precrack stage for the welded joints. The actual crack length can be determined after breaking the specimen at the end of the test. The measured and actual crack length have less than 2% difference.

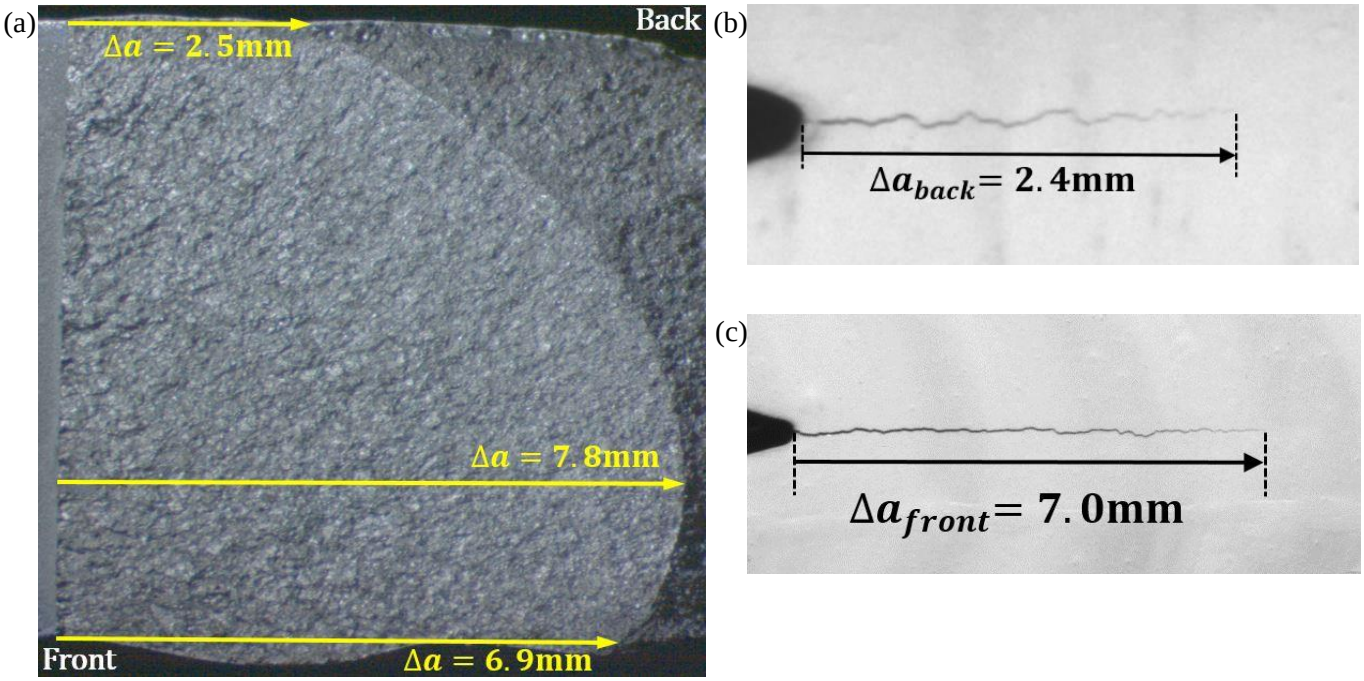

Fig. 4. (a) Top view of actual crack length obtained after the test. Measured crack length obtained during the test (b) back view (c) front view, at the end of the precrack stage.

2.3. Stress intensity factors for CTS welded specimen

Since the equations at hand for the SIFs of CTS specimen [28] are only valid for the straight crack (i.e. the direction of the crack growth does not change) and also they do not consider the weld geometry, so, a 3D simulation for several crack geometries was performed by the finite element method. The stress intensity factors, K_{I} and K_{II}, were then calculated for all the experiment

conditions by numerical simulation of the CTS specimen under mixed mode fatigue loading. Details of the numerical simulation have been completely explained in Section 3.2.2.

The equivalent stress intensity factor K_{eq} has been introduced for considering mode I and mode II simultaneously. Richard proposed Eq. (1) for the calculation of K_{eq} [29]:

$$K_{\mathrm{eq}} = \frac{K_{\mathrm{I}}}{2} + \frac{1}{2}\sqrt{K_{\mathrm{I}}^2 + 4(\alpha_1 K_{\mathrm{II}})^2} \tag{1}$$

where $\alpha_1 = 1.155$. Furthermore, the cyclic equivalent stress intensity factor, ΔK_{eq}, is:

$$\Delta K_{\mathrm{eq}} = \frac{\Delta K_{\mathrm{I}}}{2} + \frac{1}{2}\sqrt{\Delta K_{\mathrm{I}}^2 + 4(\alpha_1 \Delta K_{\mathrm{II}})^2} \tag{2}$$

Eq. (3) shows the modified form of Paris law which can be used to evaluate the behavior of mixed mode fatigue crack growth:

$$\frac{da}{dN} = C\left(\Delta K_{\mathrm{eq}}\right)^n \tag{3}$$

where C and n are material constants.

In mixed mode experiments, the maximum and minimum uniaxial fatigue loads applied in different loading angles were chosen in such a manner to give an equivalent stress intensity factor of approximately 8 MPa$\sqrt{\mathrm{m}}$ for the base metal and 9 MPa$\sqrt{\mathrm{m}}$ for the welded joint immediately after precrack growth started.

The overload ratio is defined according to Eq. (4):

$$R^{ol} = \frac{K_{eq}^{ol}}{K_{max}^{Bl}} \tag{4}$$

where K_{eq}^{ol} can be calculated using Eq. (1) and K_{max}^{Bl} denotes the maximum SIF of the baseline loading. In mixed mode overload experiments, the applied overload was chosen to have an overload ratio R^{ol}, of 1.8. The maximum baseline load (F_{max}^{Bl}) and baseline load ratio (R^{Bl}) were 5.2 kN and 0.1, respectively.

3. Mixed mode fatigue crack growth

3.1. Experimental results

It was observed that the fatigue crack growth direction changes immediately from the precrack orientation as the load direction changes. Also, it was observed that there is no great difference in crack deviation angle between non-welded and welded specimens. Fig. 5 shows crack growth paths for loading angle $\beta = 30°$ in welded and non-welded specimens.

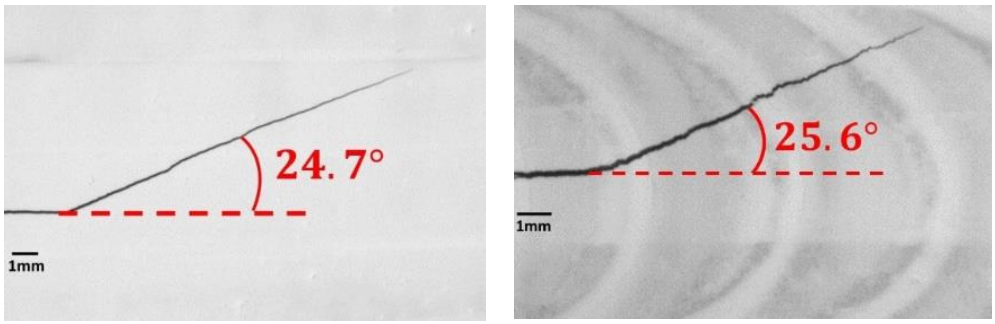

(a) (b)

Fig. 5. Crack growth paths for loading angle $\beta = 30°$ in (a) non-welded specimen (b) welded specimen.

Shahani et al. [24] showed that using Gaussian function instead of incremental polynomial method (proposed by standard ASTM E647 [30]) for calculating the fatigue crack growth rate, generates the similar mean values with better fitting. Therefore, the Gaussian function has been employed as data reduction method to calculate FCGRs for all the tests. This function is defined as [28].

$$a_i = d_1 e^{-\left(\frac{N_i - b_1}{c_1}\right)^2} + d_2 e^{-\left(\frac{N_i - b_2}{c_2}\right)^2} + d_3 e^{-\left(\frac{N_i - b_3}{c_3}\right)^2} + d_4 e^{-\left(\frac{N_i - b_4}{c_4}\right)^2} \quad (5)$$

where b_i, c_i and d_i are the regression parameters which are determined by the least squares method. Fig. 6 shows the fatigue crack growth rate of welded joints subjected to mixed mode constant amplitude loading in terms of the equivalent stress intensity factor range.

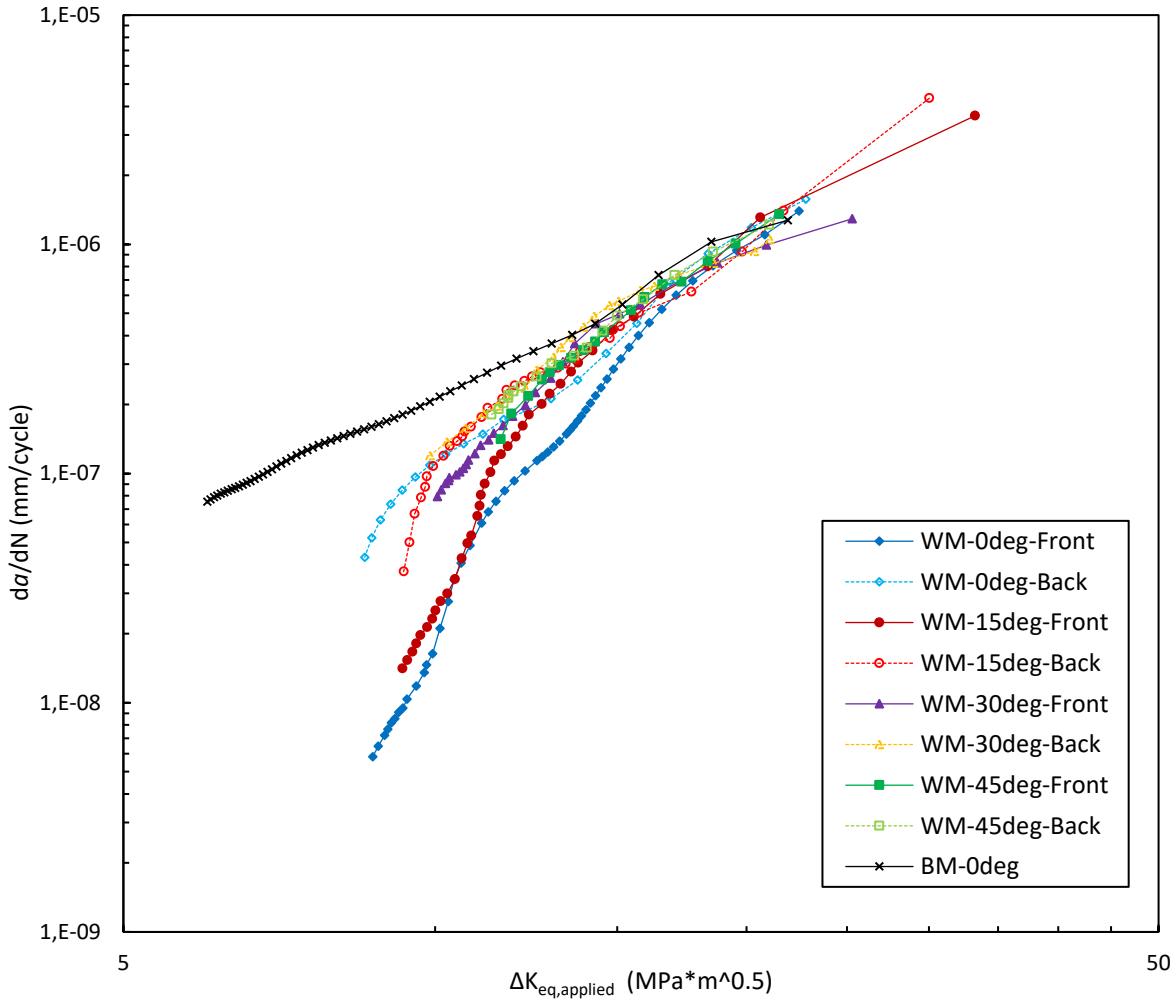

Fig. 6. FCGR of the welded specimens subjected to mixed mode constant amplitude loading.

Fig. 7 shows the fatigue crack growth rate of welded joints in comparison with base metal specimens for various mode mixities.

As can be seen from Figs. 6 and 7, at the first stage of crack growth for the same mode mixity, the FCGR in welded joint is lower than that in base metal. This is because of the compressive residual stress perpendicular to the initial crack plane by the welding process which decreases the fatigue crack growth rate. The effect of residual stress is more obvious in pure mode I condition (Fig. 7a). By increasing mode mixity the effect of the residual stress on the FCGR decreases rapidly, since the crack grows far from the weld zone because of crack deviation. Also, it can be seen that the FCGRs of specimens after a while became almost equal to each other which can be inferred that residual stress was gradually released by crack growth. In addition, in all welded specimens, the FCGR at the back side is greater than the front side. It may be due to different

distribution of welding residual stress at front and back sides of the welded specimens. So, finite element simulation is performed to investigate the effect of welding residual stress.

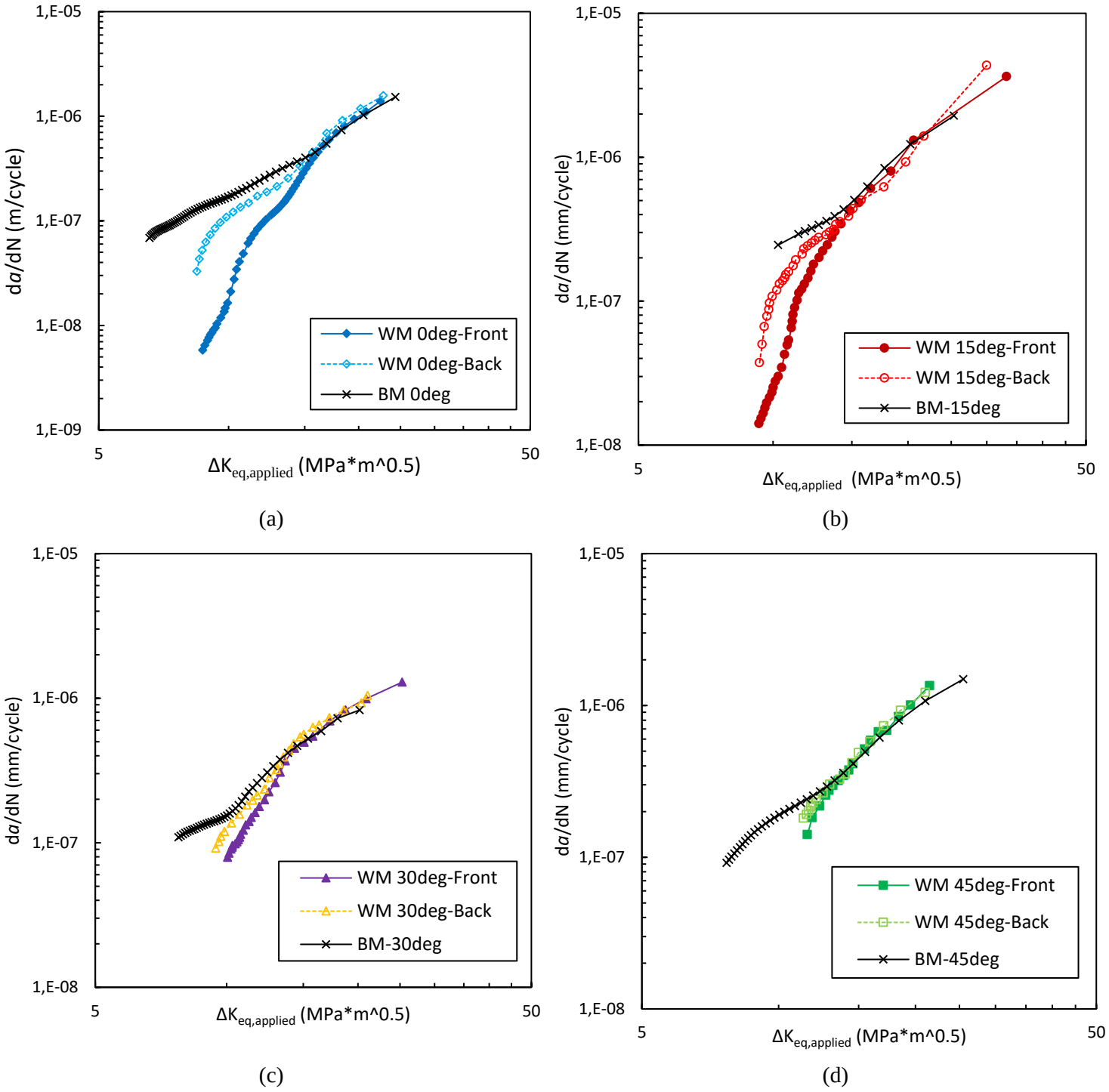

Fig. 7. Fatigue crack growth rate of WM and BM specimens versus $\Delta K_{\mathrm{eq,applied}}$.

3.2. Finite element analysis

In order to obtain the exact value of stress intensity factors including residual stress effect, 3D finite element simulation was performed using two software, Abaqus 6.14-2 [27] and Zencrack [31]. At first, welding simulation was conducted to achieve distribution of residual stress and then crack growth simulation was performed.

3.2.1. Welding simulation

3D finite element simulation of the welding process was conducted using Abaqus. The sequentially coupled thermomechanical analysis was accomplished, in which heat transfer analysis was followed by mechanical analysis. It means, a thermal analysis was firstly performed to achieve the temperature history of the plate. Thereafter, the temperature history was incrementally applied to the mechanical analysis in order to determine the residual stresses. That is, in mechanical analysis the temperatures of nodes were read from an output file which produced during thermal analysis. Fig. 8 illustrates the steps of welding simulation.

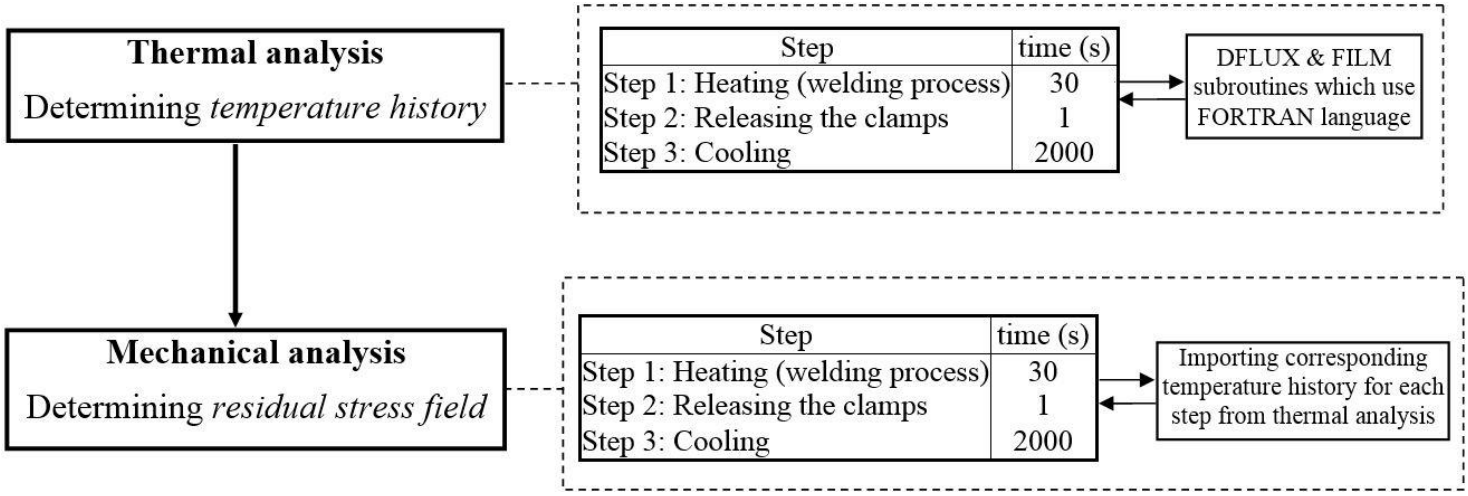

Fig. 8. Steps of welding simulation.

Hexagonal quadratic heat transfer elements (DC3D20) were employed for the thermal analyses. The size of the meshes employed in the mechanical and thermal models was identical. In the mechanical analyses, hexagonal quadratic elements with reduced integration (C3D20R) were used. A mesh convergence study on the weld centerline was performed by changing the size of elements. It was found that the elements with the size of 0.2 mm near the welding zone, would provide

converged temperatures as well as residual stresses. Eventually, the model was discretized using 41968 elements and 188023 nodes.

Fig. 9 and Table 4 show the material properties employed in the FE analysis. Tensile tests were carried out under various temperatures to obtain variation of mechanical properties in terms of temperature (Fig. 9b). At high temperatures equal to the melting temperature, the value of Young's modulus nearly approaches zero and subsequently the problem diverges due to numerical instabilities. In order to solve mentioned problem, the value of Young's modulus at melting point was considered as 0.00007 GPa. The physical properties of Al5083-H116 available at the literature [32] were used instead of Al5083-H111 (Fig. 9a), since physical properties of 5xxx series aluminum alloy do not vary in the wide range.

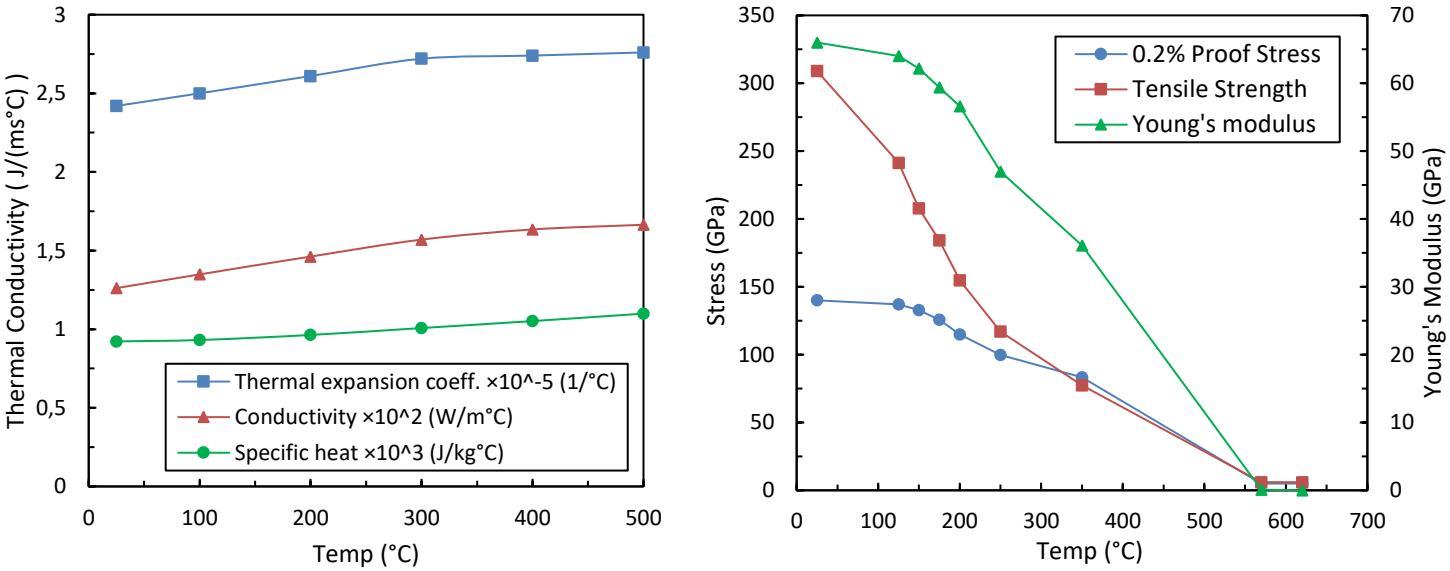

(a) (b)

Fig. 9. (a) The physical and thermal properties of Al5083-H116 [32] (b) The mechanical properties of Al5083-H111 obtained from present investigation.

Table 4. Material properties of aluminum alloy [33].

Density (kg/m^3)	2640
Latent heat (J/kg)	300000
Melting range $(°C)$	570-620
Poisson's ratio	0.33

The welding process parameters presented in Table 2 were employed in the thermal analysis of welding. A moving distributed heat flux was applied as a heat source on the front surface of the plate. According to the Friedman model [34], it was assumed that the heat source with a circular shape is perpendicularly applied to the surface. The heat flux should be calculated at a certain time and location on the surface of elements on which the heat flux is acted. For this purpose, a user subroutine named DFLUX, which uses the FORTRAN language was developed and included in the model. The distribution of heat flux is stated as Eq. (6) [34]:

$$q(r) = \frac{3Q}{\pi r_b^2} e^{-3(r/r_b)^2} \tag{6}$$

where Q is the input heat and it can be calculated for arc welding by the following equation [35]:

$$Q = \eta V I \tag{7}$$

where I and V are the arc current and voltage, respectively. η is the arc efficiency and was assumed to be 90% for the TIG welding process [35]. r, as illustrated in Fig. 10, is the distance between the point in which the heat flux is calculated and the center point of the heat source and it is expressed as:

$$r = \sqrt{(x - x_h)^2 + y^2} \tag{8}$$

where x_h is the location of center point of moving heat source and it can be determined at each moment by Eq. (9):

$$x_h = vt \tag{9}$$

where v is the welding speed. It can be seen that by increasing the time (t), the heat source moves on the front surface of the plate. It was determined in the subroutine that if the value of r is equal to or less than r_b, Eq. (6) is used to calculate the heat flux and if not, the heat flux is set to zero. r_b characterizes the heat input distribution and specifies the area in which 95% of the heat flux is deposited and it was set to 5.5 mm based on the weld pool size [33].

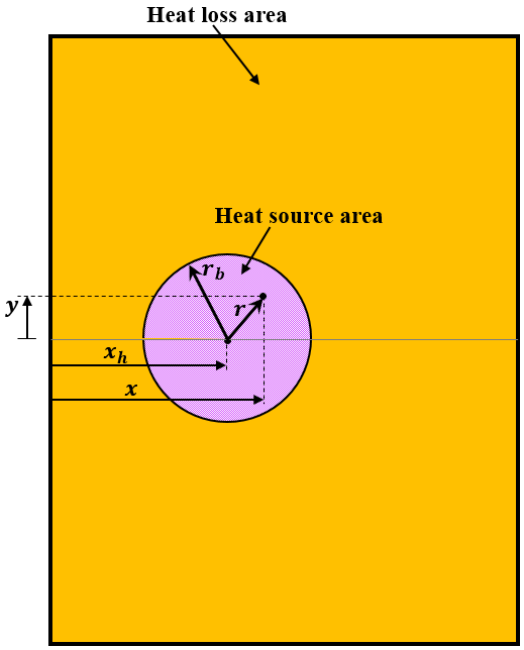

Fig. 10. Region of the heat source and heat loss.

The convection and radiation to the environment were considered as the thermal boundary conditions for all faces of the specimen except the region on which the heat source is acted. The heat loss can be evaluated by Eq. (10):

$$q = q_{\text{convection}} + q_{\text{radiation}} = h_{\text{convection}}(T_i - T_a) + \varepsilon_{\text{em}}\sigma_{\text{bol}}(T_i^4 - T_a^4) \quad (10)$$

where T_a and T_i are the ambient temperature and instantaneous temperature, respectively. $h_{\text{convection}}$ is the convection coefficient and it was set to 8 $W/m^2\,°C$. The emissivity, ε_{em}, is 0.15 for aluminum and the Stefan-Boltzman constant, σ_{bol}, is 5.67037×10^{-8} $W/m^2\,°C^4$ [36]. Also, the ambient temperature was set to 20°C.

As the heat loss area changes over the time for the front face of specimen, another subroutine, named FILM, was developed and employed with DFLUX. In the developed code, if the location under consideration is located within the circular area where the flux is acted, no heat loss occurs. Otherwise, the heat loss coefficient, which consists of both the radiation and convection coefficients, is calculated as follows:

$$h_{\text{total}} = h_{\text{convection}} + \varepsilon_{\text{em}}\sigma_{\text{bol}}(T_i^3 + T_i^2 T_a + T_i T_a^2 + T_a^3) \quad (11)$$

therefore, the total heat loss is calculated as:

$$q = h_{\text{total}}(T_i - T_a) \quad (12)$$

After the heat source reaches the end of the specimen, the specimen was cooled down until the steady state. Fig. 11a shows the distribution of temperature in the specimen due to the moving heat source at t=10s. It can be seen that the maximum temperature occurs on the front surface and at the center of the heat source. Fig. 11b illustrates the temperature history at different locations on the middle section of the specimen. As can be seen from Fig. 11, the temperature decreases by moving away from the weld centerline.

(a)

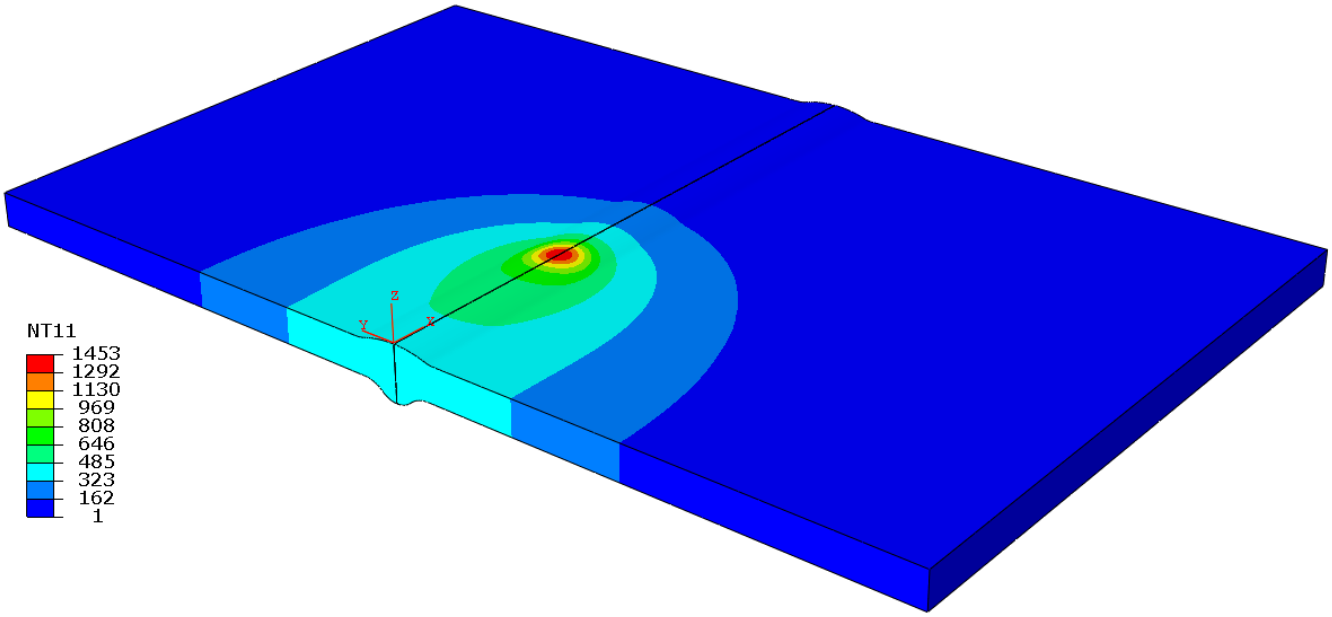

(b)

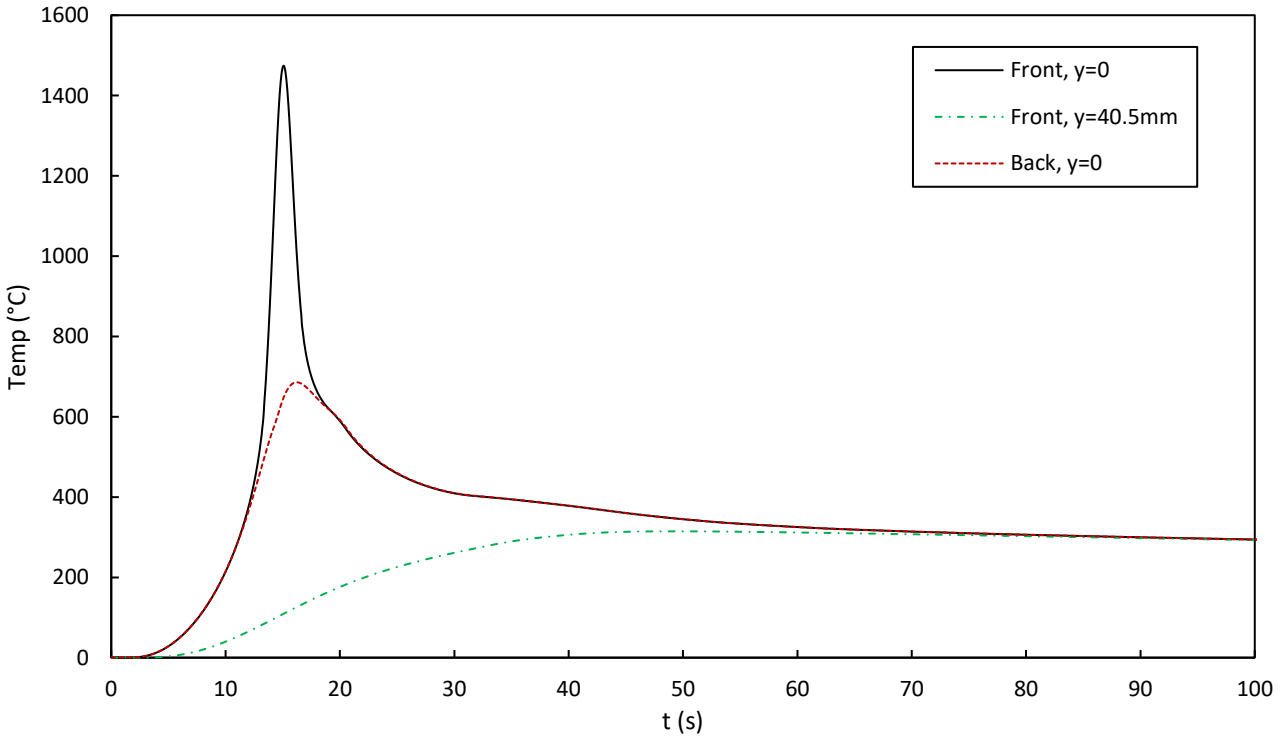

Fig. 11. (a) Distribution of temperature during motion of the heat source at t=10s. (b) Temperature history at x=45mm.

In order to verify the developed subroutines in thermal model, the problem performed by Fanous et al. [35], was modeled. A plate with a width of 50 mm (y direction), length of 100 mm (x direction), and thickness of 2.5 mm was considered. The welding speed, arc voltage, arc current and arc efficiency were 2 mm/s, 24 V, 30 A and 90%, respectively. The material used was Inconel Alloy 600. Fig. 12 shows the results of thermal analysis for two different points on the top surface at the middle of the plate (x=50 mm). Good agreement is observed between the thermal results of present study and those of Fanous et al. [35].

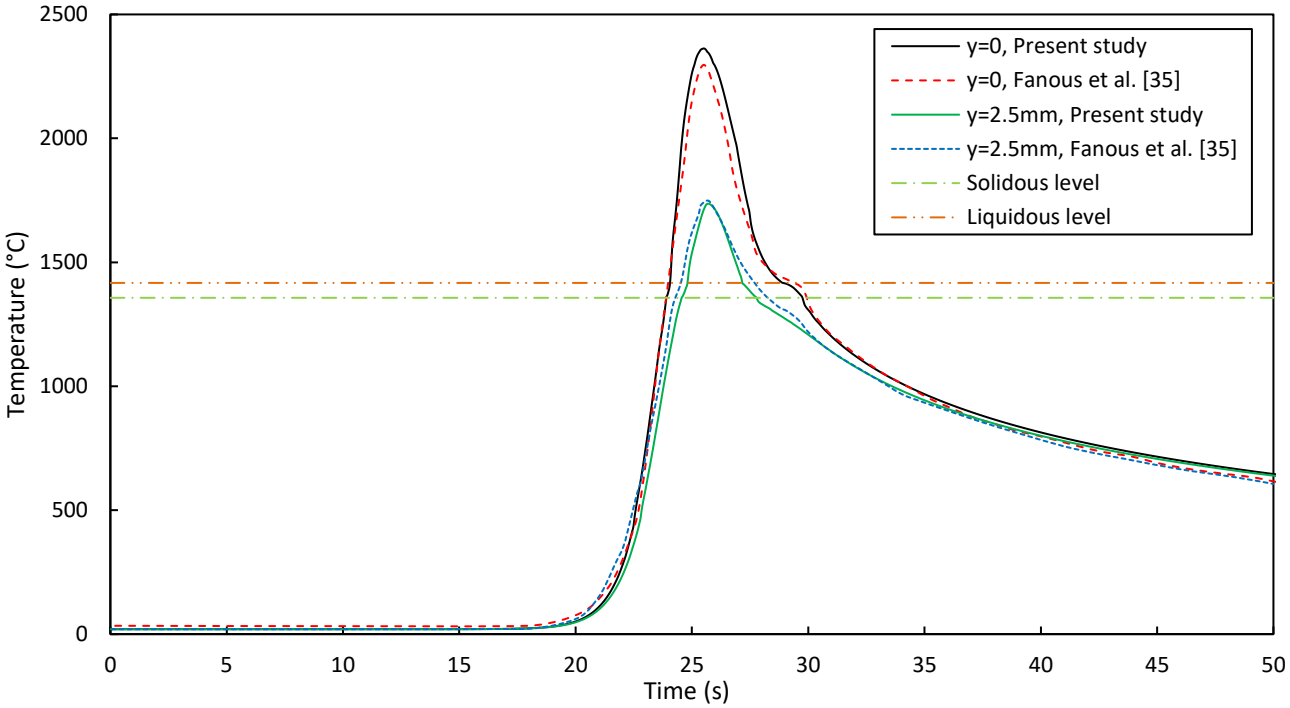

Fig. 12. Verification of thermal analysis for two different points on the top surface at x=50 mm.

The thermal elasto-plastic material model, on the basis of the isotropic strain hardening rule and the von Mises yield criterion, was considered. Since the thermal elasto-plastic analysis is a non-linear problem, an incremental calculation technique was used to solve the problem.

The restrictions due to the clamps during welding process should be considered in the FE model. For this purpose, the surfaces under clamping force as shown in Fig. 13, were fixed in the x, y and z directions during the heating step (step 1). In the next step the restrictions of the clamped surfaces were removed. In order to prevent the rigid body motion of the specimen, the displacement of four nodes on planes far from the weld line was constrained in the x or z directions as shown in Fig. 13.

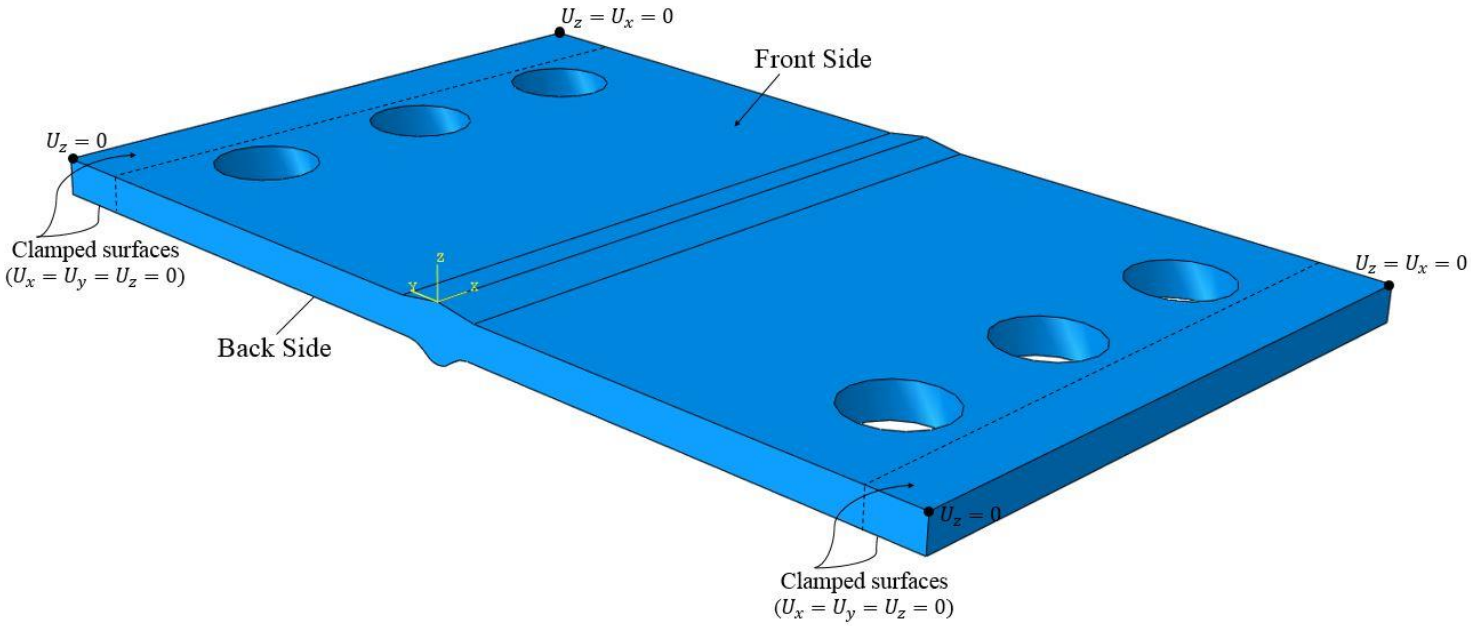

Fig. 13. Boundary conditions of the specimen in mechanical analysis.

After cooling step, i.e. step 3, another step was defined to create holes in the specimen using element death technique.

Fig. 14 shows the resultant transverse component of stress (S_{22}) on the front surface at the end of each step. It should be mentioned that S_{22} is perpendicular to the crack plane and so it plays an important role during crack growth.

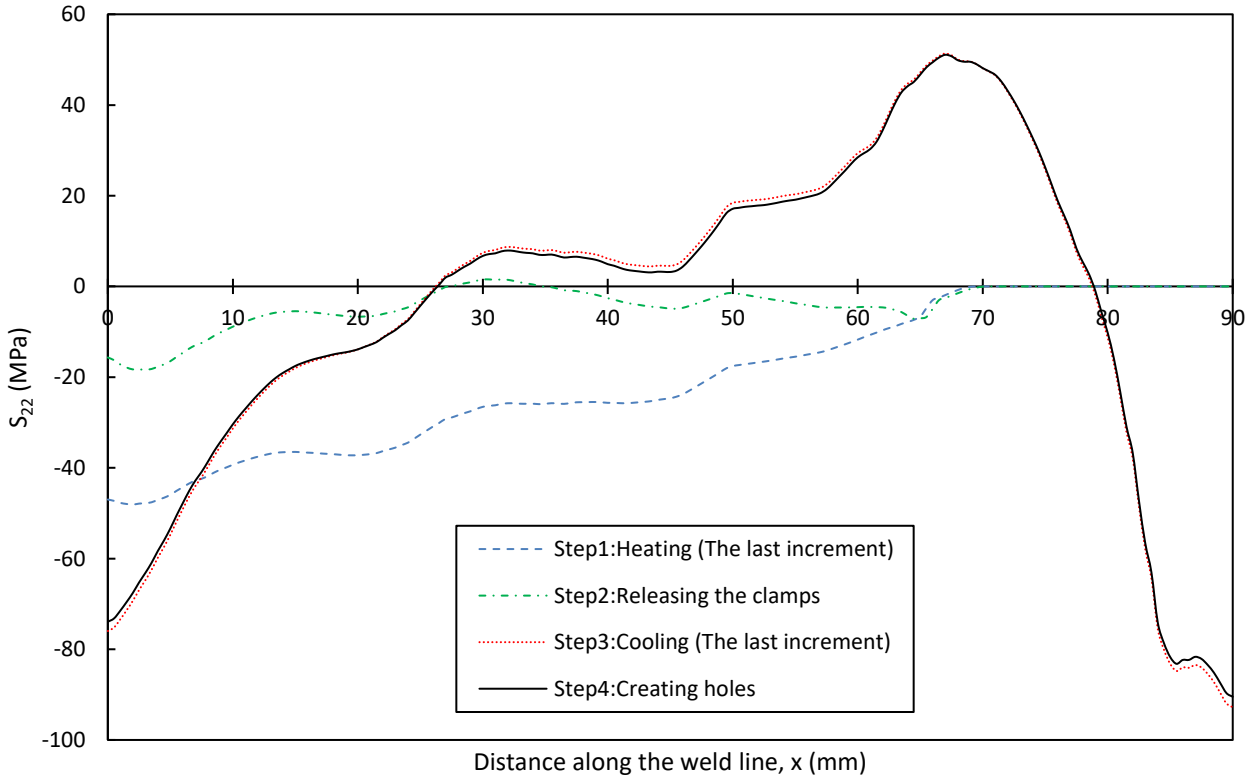

Fig. 14. Distribution of transverse stress on the front surface along the weld centerline, $y = 0$mm.

As can be seen from Fig. 14, in the last increment of the heating step the stress in regions with elevated temperature ($x > 60\text{mm}$) is noticeably low. By releasing the clamps (step 2), the stress decreases due to removing the restriction especially in the y direction. By cooling down the specimen into the ambient temperature, the absolute amount of stress increases and stress remains in the specimen as the residual stress. The residual stress in the specimen appears as a result of interaction of elastic strains with plastic strains accumulated during welding process. The residual stress is self-balanced. So, it is tensile in some regions and compressive in others. In other words, the welding residual stress satisfies the self-equilibrating condition between the tensile and compressive regions in a welded joint. It is seen that the amount of residual stress in the specimen tested is considerable and it should be taken into account. As can be observed from Fig. 14, by creating the holes in the specimen, the pattern of residual stress distribution does not change considerably near the weld centerline.

3.2.2. Crack growth simulation

In order to obtain the precise value of the SIFs including residual stress effect, three dimensional simulation of fatigue crack growth was performed using Zencrack commercial software linked to Abaqus.

Zencrack replaces the regular elements at the position of crack in the un-cracked model by the crack blocks containing singular wedge elements (Fig. 15b). Residual stresses obtained from welding simulation (Section 3.2.1) were imported to the crack growth analysis as predefined field. Zencrack uses maximum energy release rate criterion for calculating crack growth direction. The magnitude and direction of maximum energy release rate at each node of the crack front are calculated and then the crack front is updated accordingly. This procedure will be repeated until the crack size or the number of cycles reaches a prescribed value.

The point loads, as shown in Fig. 15a, are related to the applied uniaxial load F according to the following equations [18]:

$$F_1 = F_6 = F\left(\frac{1}{2}\cos\beta + \frac{c}{b}\sin\beta\right) \quad (13)$$

$$F_2 = F_5 = F\sin\beta \quad (14)$$

$$F_3 = F_4 = F\left(\frac{1}{2}\cos\beta - \frac{c}{b}\sin\beta\right) \quad (15)$$

To apply the loads, as shown in Fig. 15a, reference points (RP) were placed at the center of the holes of the specimen and each one was coupled to half of circumference of the hole.

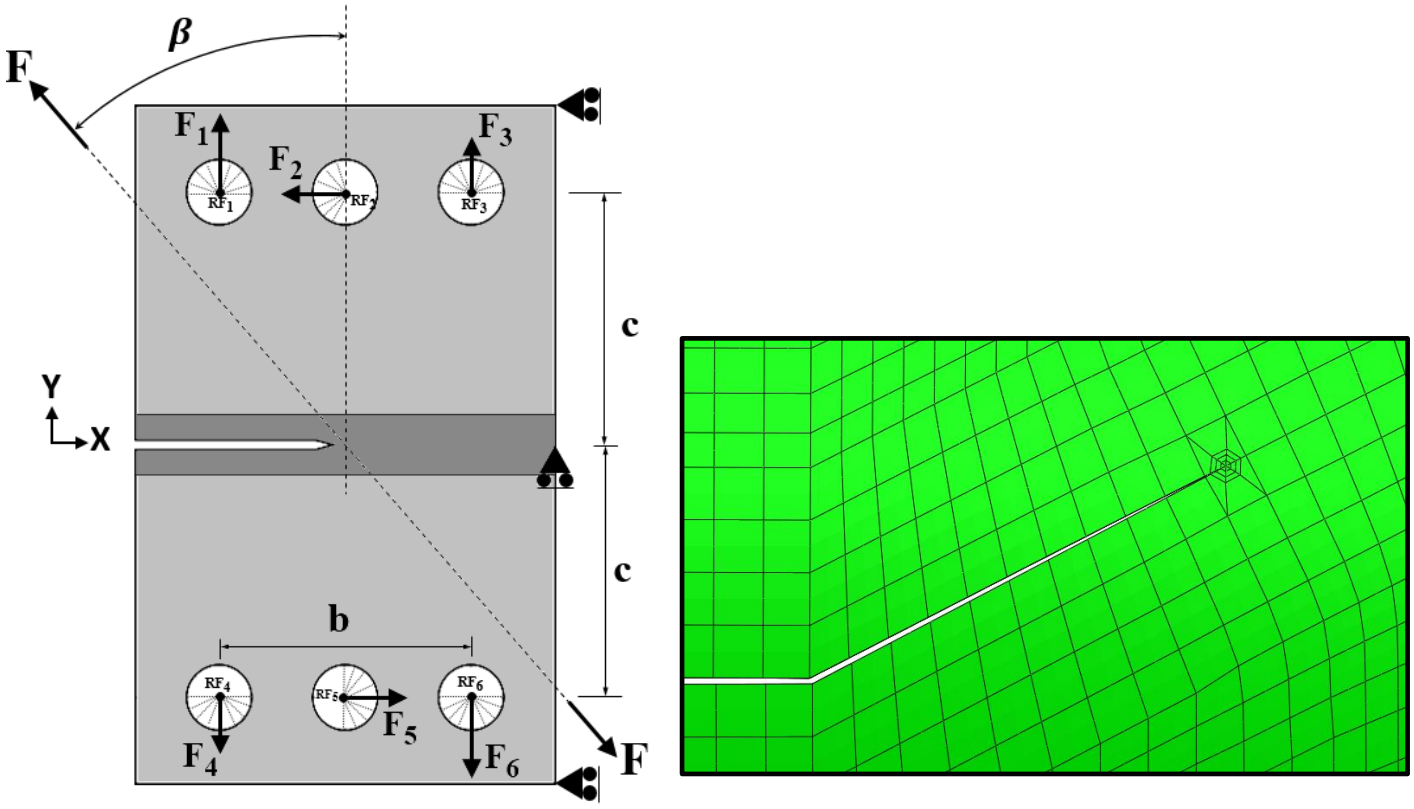

(a) (b)

Fig. 15. (a) Boundary conditions and loading applied to the specimen (b) Mesh pattern employed for FE simulation including singular elements at the crack front ($\beta = 30^{\circ}$).

The material behavior was assumed to be linear elastic. C and n of Paris relation were set to 16.5×10^{-10} and 2.03 which were obtained from curve fitting to data of BM experiment (Fig. 6) and they were employed for all other cases. Simulations have been done for β =0, 15, 30 and 45°. Fig. 16 shows the comparison of the crack growth paths obtained from experiments and numerical simulations for BM and WM specimens.

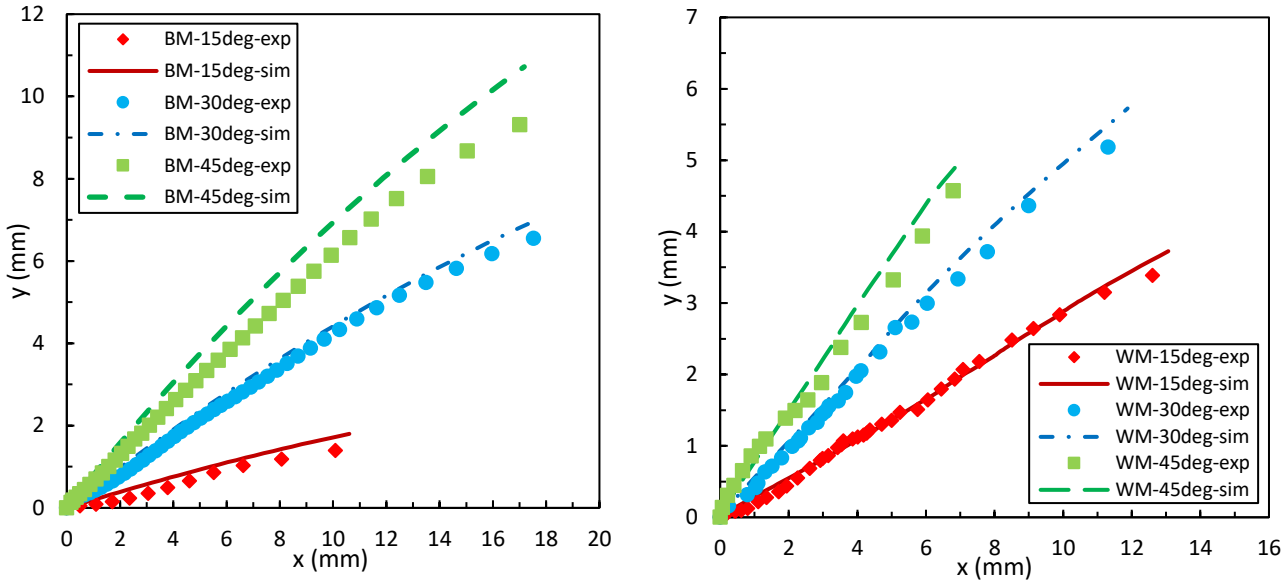

(a) (b)

Fig. 16. Experimental and numerical crack growth paths for BM and WM specimens.

As can be seen from Fig. 16, there is a good agreement between the measured and predicted crack growth paths. For the case of BM specimen under $\beta = 45^{\circ}$ loading, the difference between the predicted and measured path increases slightly as the crack grows. This difference is related to the rolling direction. Richard et al. [37] showed that the crack has a tendency to change its orientation from predicted path to the rolling direction. In welded specimens, the rolling direction disappears as a result of melting and recrystallization at the weld zone.

3.3. Effective stress intensity factor

As previously shown in Fig. 14, the amount of residual stress in the specimen tested is considerable and it should be taken into account in the FCGR. In order to consider the effect of residual stress in the fatigue crack growth rate, the effective stress intensity factor range is defined as Eq. (16):

$$\Delta K_{\mathrm{I,eff}} = \begin{cases} \left(K_{\mathrm{I,applied,max}} + K_{\mathrm{Res}}\right) - \left(K_{\mathrm{I,applied,min}} + K_{\mathrm{Res}}\right) & K_{\mathrm{I,applied,min}} + K_{\mathrm{Res}} > 0 \\ \left(K_{\mathrm{I,applied,max}} + K_{\mathrm{Res}}\right) & K_{\mathrm{I,applied,min}} + K_{\mathrm{Res}} \le 0 \end{cases} \tag{16}$$

where $K_{\mathrm{I,applied}}$ and K_{Res} are SIFs caused by the external applied load and by the residual stress, respectively. Then, the cyclic equivalent stress intensity factor, i.e. Eq. (2), is modified as follows:

$$\Delta K_{\mathrm{eq,eff}} = \frac{\Delta K_{\mathrm{I,eff}}}{2} + \frac{1}{2}\sqrt{\Delta K_{\mathrm{I,eff}}^2 + 4(\alpha_1 \Delta K_{\mathrm{II}})^2} \tag{17}$$

It should be noted that the residual stress affects only mode I stress intensity factor and it does not contribute to mode II stress intensity factor, so it is merely included into the K_{I}. Fig. 17 illustrates fatigue crack growth rates in terms of $\Delta K_{\mathrm{eq,eff}}$ for various loading angles.

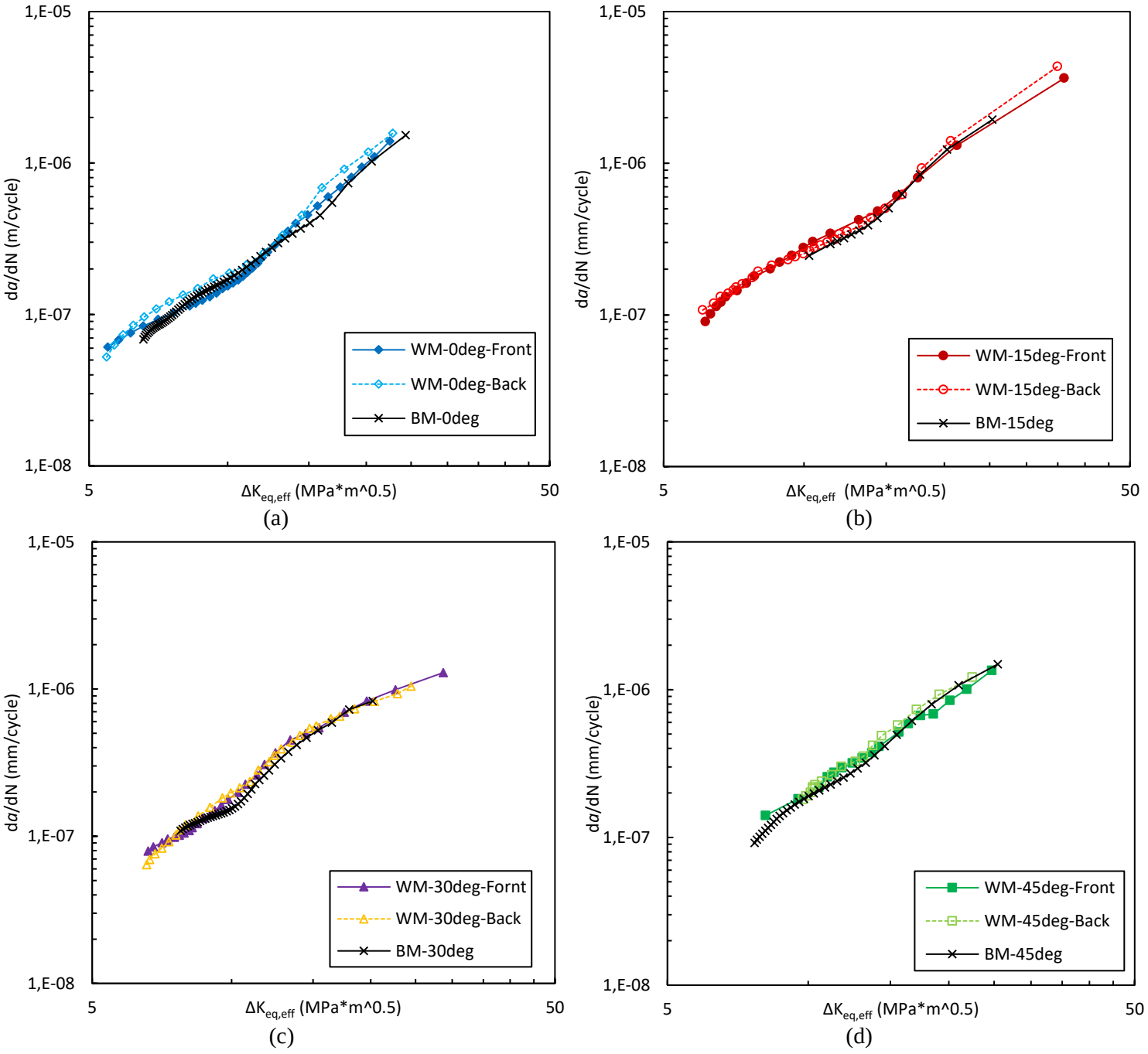

Fig. 17. Crack growth rate versus $\Delta K_{\mathrm{eq,eff}}$ for (a) $\beta = 0^{\circ}$ (b) $\beta = 15^{\circ}$ (c) $\beta = 30^{\circ}$ (d) $\beta = 45^{\circ}$.

Comparing the two Figs. 17 and 7, it is clearly observed that in each loading angle, when the residual stress effect is included in FCGR curves, FCGR data for BM and WM specimens tend to fall within a very narrow scatter band. In other words, $\Delta K_{\mathrm{eq,eff}}$ is satisfactorily able to correlate FCGR of welded specimen with that of BM specimen.

4. Fatigue crack growth of welded joint subjected to overload

In the second stage of present research, the effect of mixed mode single overload on the fatigue crack propagation of welded specimens is investigated. The experimental procedure was formerly described in Section 2.2.

By applying the overload, a retardation occurs in fatigue crack growth. The retardation behavior is characterized by two parameters named as the delay cycles (N_d) and the delay length (a_d). These two parameters are schematically illustrated in Fig. 18. As shown in Fig. 18, retardation stops when the FCGR after applying the overload becomes equal to the FCGR prior to applying the overload.

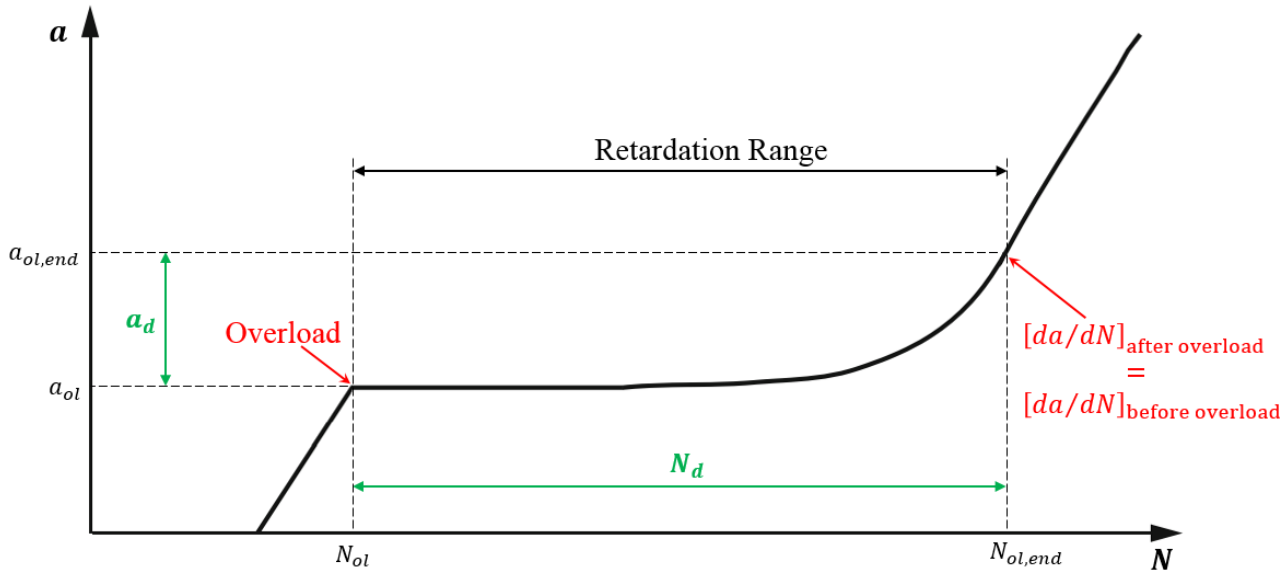

Fig. 18. Retardation parameters shown on a typical $a - N$ curve.

4.1. Effect of PWHT on retardation caused by overload

Prior to presenting results of mixed mode overload for as-welded specimens, the effect of post weld heat treatment on retardation of crack growth has been studied for pure mode I overload as illustrated in Fig. 19.

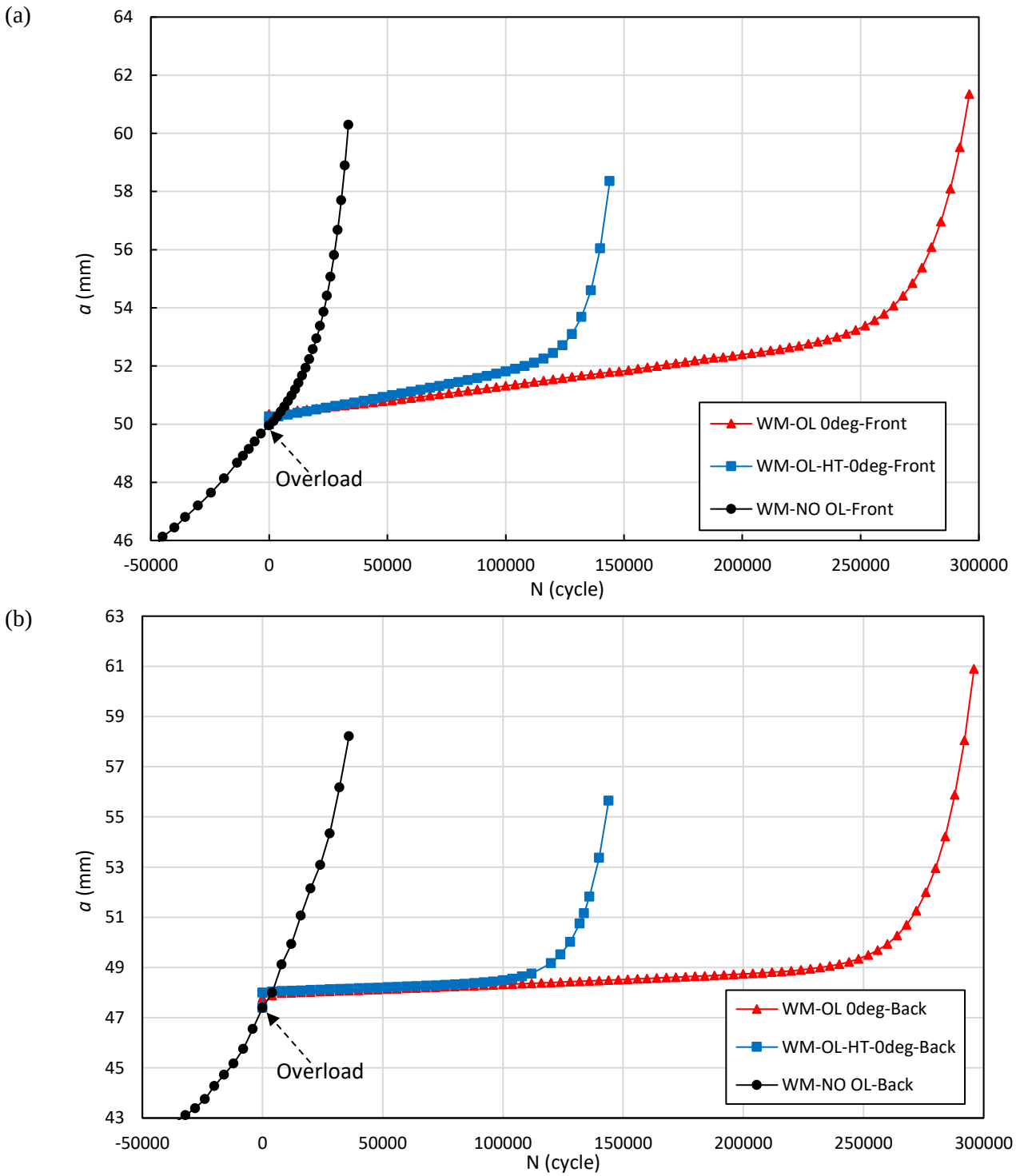

Fig. 19. The effect of post weld heat treatment on retardation of crack growth caused by pure mode I overload.

It can be seen from Fig. 19 that post weld heat treatment leads to a significant reduction in retardation. It was numerically shown (Section 3.2.1) that compressive residual stress appears around the crack front due to welding process. This compressive residual stress helps to increase crack closure caused by the overload. On the other hand, residual stress is released by post weld heat treatment and subsequently the retardation decreases.

4.2. Retardation caused by mixed mode overload

Fig. 20 shows the influence of mixed mode I+II single overload on the fatigue crack growth of as-welded specimens for various overload angles.

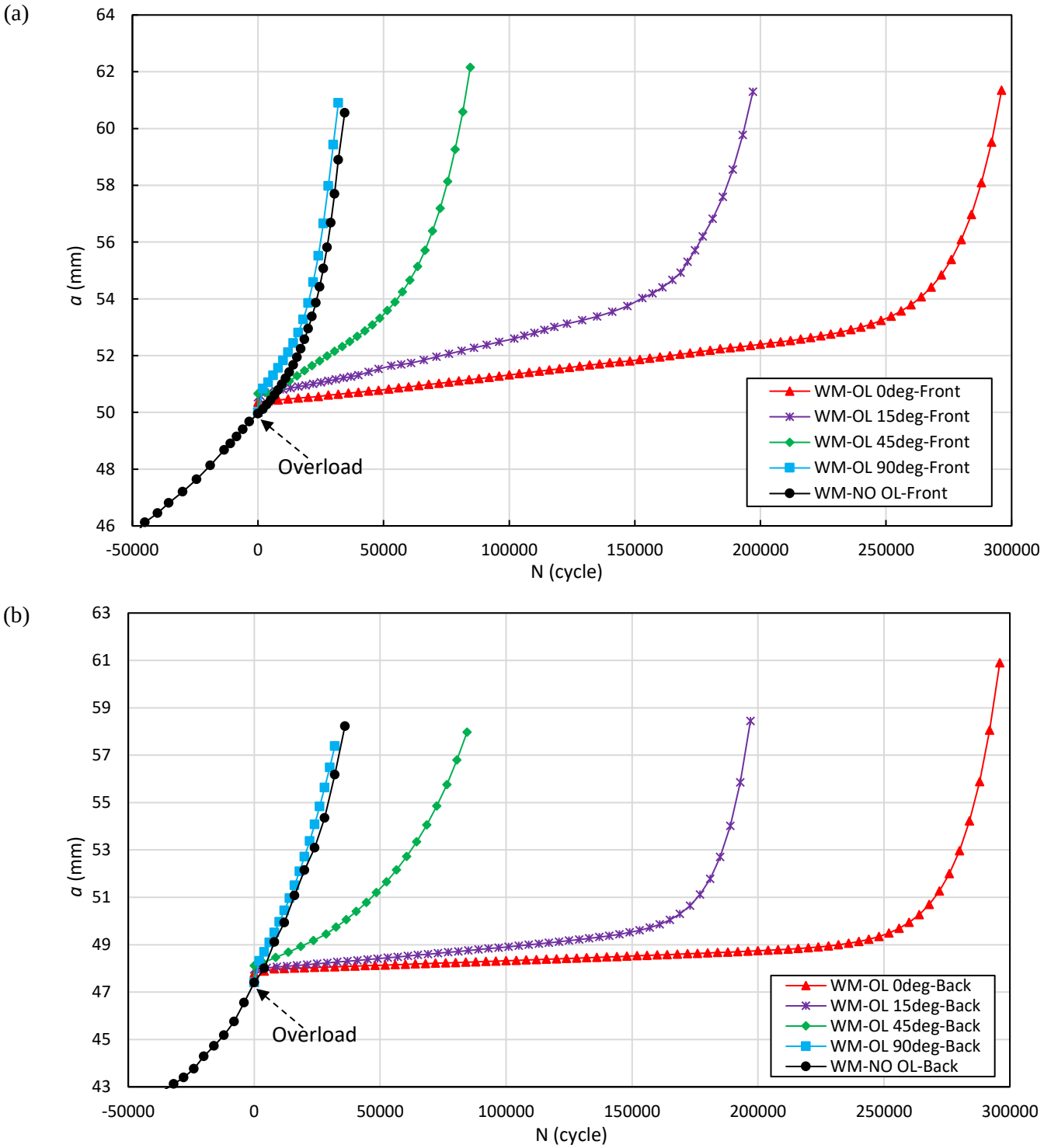

Fig. 20. Influence of mixed mode single overload on the fatigue crack growth of the welded specimens for various overload angles at (a) front side (b) back side.

As can be seen from Fig. 20, pure mode I overload created the largest retardation. As the fraction of mode II in the overload increases, the amount of retardation decreases. Shahani et al. [24] justified this by the plastic deformation caused by mixed mode overload. They showed that the plastic zone around the crack tip rotates by increasing the fraction mode II of overload and also its size becomes smaller in the vertical direction with respect to the crack plane (y-direction). The compressive residual stress around the crack tip decreases by decreasing plastic deformation in the y-direction and subsequently, the amount of retardation decreases as the shear portion of the mixed mode overload increases.

4.3. The modified Wheeler retardation model

Shahani et al. [24] proposed two models to predict crack growth retardation of non-welded structures subjected to mixed mode overload based on the Wheeler retardation model. The retarded fatigue crack growth rate is stated as follows:

$$\left(\frac{da}{dN}\right)_{\text{Retarded}} = \left(C_p\right)_i^* \left(\frac{da}{dN}\right)_{\text{CA}} = \left(C_p\right)_i^* (C\Delta K_i{}^n) \tag{18}$$

where $(da/dN)_{\text{CA}}$ is FCGR of constant amplitude loading and C and n are constants of Paris relation. $\left(C_p\right)_i^*$ is mixed mode retardation parameter and is determined according to the following equation:

$$\left(C_p\right)_i^* = \begin{cases} \left(\frac{r_{p,i}}{a_{ol}+r_{p,ol}-a_i}\right)^{m^*} & a_i + r_{p,i} < a_{ol} + r_{p,ol} \\ 1 & a_i + r_{p,i} \geq a_{ol} + r_{p,ol} \end{cases} \tag{19}$$

where m^* is the mixed mode exponent, a_{ol} denotes the crack length when the overload was applied, $r_{p,ol}$ denotes the size of the plastic zone produced by the mixed mode overload, a_i denotes the crack length corresponding to the i^{th} load cycle and $r_{p,i}$ denotes the size of current plastic zone at a_i (Fig. 21). By reaching the boundary of the current plastic zone to the boundary of the overload plastic zone, retardation ceases. At this point, the current FCGR becomes equal to the FCGR prior to applying the overload.

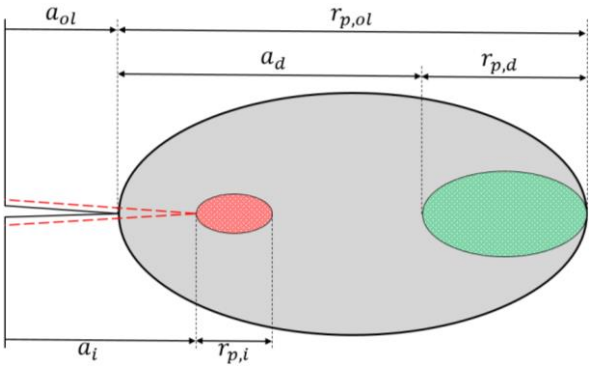

Fig. 21. Definition of plastic zone size employed in the Wheeler model.

The plastic zone size is determined as follows [24,38]:

$$r_p = \alpha \left(\frac{K_{eq}}{S_y}\right)^2 \tag{20}$$

where α is the plastic zone size factor, S_y is the yield stress and K_{eq} is obtained from Eq. (1).

The mixed mode exponent, m^*, is defined according to the model used as follows [24]:

Model I: $\frac{m^*}{m_I} = A\left(\frac{K_I^{ol}}{K_I^{ol}+K_{II}^{ol}}\right) + B$ (21)

Model II: $m^* = m_I\left(\frac{K_I^{ol}}{K_I^{ol}+K_{II}^{ol}}\right)$ (22)

where m_I is the Wheeler exponent for specimen under pure mode I overload. A and B are material constants which are achieved from experiment.

It was shown that the model I predicts the retardation more accurately than model II (especially in pure mode II overload) [24]. However, it contains two constants which should be obtained from several experiments. Nevertheless, only one experiment is needed to calculate mixed mode exponent in model II. The application of these two models proposed for non-welded specimens is examined for welded joints used in the present study.

The mixed mode exponent (m^*) and plastic zone size factor (α) can be calculated from a practical method which was firstly proposed by Sheu et al. [39] for pure mode I overload. Later, Shahani et al. [24] employed this method for non-welded specimen under mixed mode overload.

Plastic zone size factor (α) can be determined with the aid of the delay length (a_d), shown in Fig. 21, as follows:

$$a_d = r_{p,ol} - r_{p,d} = \alpha\left[\left(\frac{K_{eq}^{ol}}{S_y}\right)^2 - \left(\frac{K_I^d}{S_y}\right)^2\right] \quad (23)$$

where $r_{p,ol}$ is size of the plastic zone caused by overload, K_I^d is the maximum SIF corresponding to crack length of $a = a_{ol} + a_d$ and $r_{p,d}$ is size of the plastic zone at K_I^d. The delay length (a_d) is determined based on the experimental results (Fig. 18).

The mixed mode exponent (m^*) can be obtained by employing another retardation parameter, i.e. the delay cycles (N_d). An iterative procedure, as shown in Fig. 22, is needed to calibrate the mixed mode exponent. In particular case of pure mode I overload $m^* = m_I$.

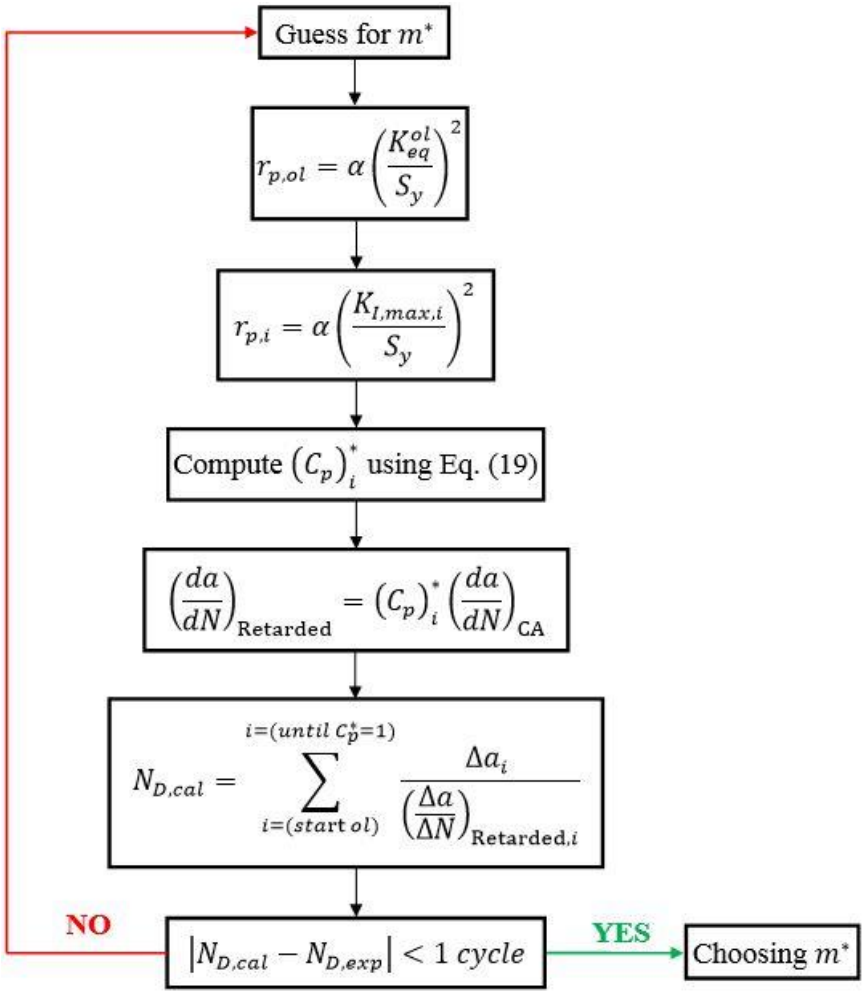

Fig. 22. Procedure used for calculating the mixed mode exponent.

Table 5 presents the values of the mixed mode exponent (m^*) obtained from experimental results in comparison with the values predicted by the two models proposed by Shahani et al. [24]. Calculations were performed for both sides of the specimen.

Table 5. Values of m^* obtained from experimental results and two models for various overload angles.

β	Front Side					Back Side				
	Exp.	Model I		Model II		Exp.	Model I		Model II	
		Value	Error (%)	Value	Error (%)		Value	Error (%)	Value	Error (%)
0°	2.32	1.96	15.5	2.32	0	2.48	2.08	16.1	2.48	0
15°	1.54	1.64	6.5	1.98	28.6	1.76	1.83	4.0	2.21	25.6
45°	0.69	1.15	66.7	1.45	110.1	0.86	1.36	58.1	1.69	96.5
90°	0	0.19	100	0	0	0	0.17	100	0	0

The normalized mixed mode exponent (m^*/m_I) versus mode mixity $(K_I/(K_I+K_{II}))$ is illustrated in Fig. 23 for both sides of the specimen.

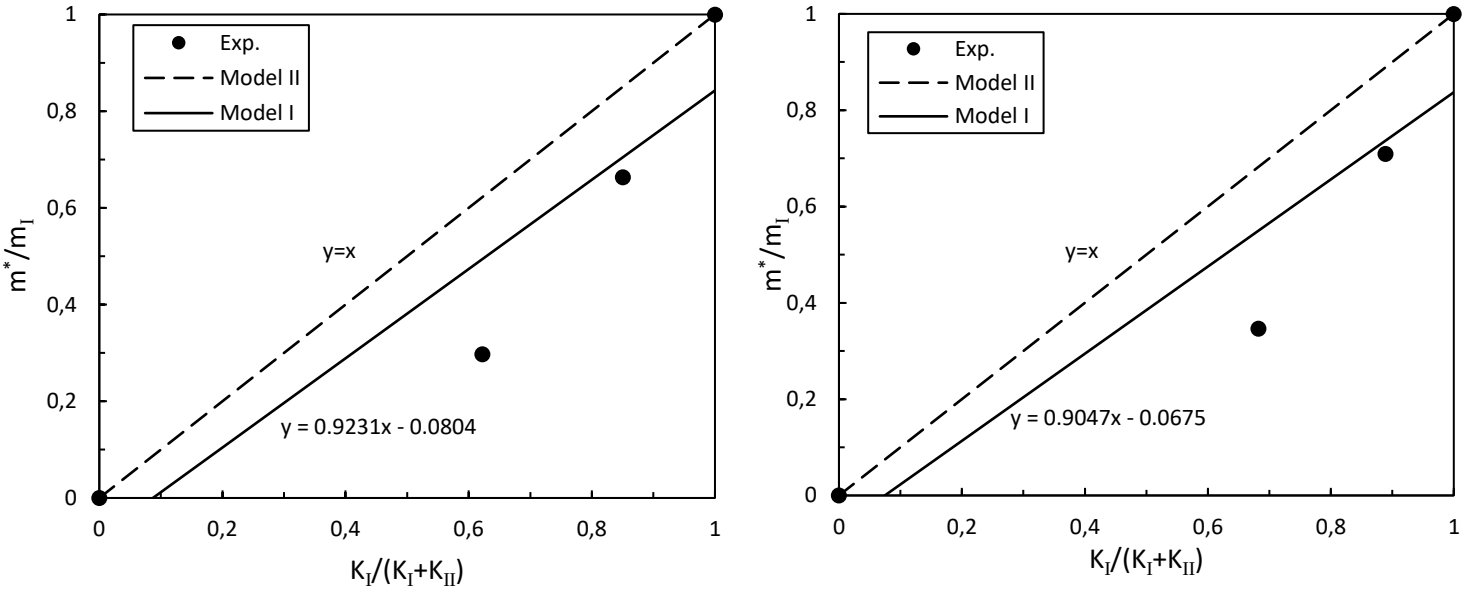

(a) (b)

Fig. 23. Normalized mixed mode exponent in terms of mode mixity for (a) front side and (b) back side of the specimen.

As can be seen from Fig. 23 and Table 5, the proposed models for predicting mixed mode exponent in non-welded specimen, are not accurate for welded joints.

4.4. Improvement of the modified Wheeler retardation model

The welding residual stress has not been considered in calculation of mixed mode parameter as well as mode mixity in the models proposed by Shahani et al. [24]. Also, it was shown that the residual stress affects the FCGR of the welded joints. For this purpose, the models are modified by replacing SIFs in all previous equations with the effective stress intensity factor ($K_{\mathrm{I,eff}}$) defined in Eq. (24) which includes the effect of welding residual stress:

$$K_{\mathrm{I,eff}} = K_{\mathrm{I,applied}} + K_{\mathrm{Res}} \tag{24}$$

So, the two models for calculating mixed mode exponent are rewritten as follows:

$$\text{Modified Model I: } \frac{m^*}{m_I} = A\left(\frac{K_{\mathrm{I,eff}}^{\mathrm{ol}}}{K_{\mathrm{I,eff}}^{\mathrm{ol}}+K_{\mathrm{II}}^{\mathrm{ol}}}\right) + B = A\left(\frac{K_{\mathrm{I}}^{\mathrm{ol}}+K_{\mathrm{Res}}}{K_{\mathrm{I}}^{\mathrm{ol}}+K_{\mathrm{II}}^{\mathrm{ol}}+K_{\mathrm{Res}}}\right) + B \tag{25}$$

$$\text{Modified Model II: } m^* = m_I\left(\frac{K_{\mathrm{I,eff}}^{\mathrm{ol}}}{K_{\mathrm{I,eff}}^{\mathrm{ol}}+K_{\mathrm{II}}^{\mathrm{ol}}}\right) = m_I\left(\frac{K_{\mathrm{I}}^{\mathrm{ol}}+K_{\mathrm{Res}}}{K_{\mathrm{I}}^{\mathrm{ol}}+K_{\mathrm{II}}^{\mathrm{ol}}+K_{\mathrm{Res}}}\right) \tag{26}$$

As formerly noted, the residual stress contributes to the mode I stress intensity factor and subsequently it is only included into the K_{I}. By Considering the modified models and repeating the previous procedure for calculating mixed mode exponent, the updated values for mixed mode exponent can be obtained as presented in Table 6.

Table 6. Values of m^* estimated from the experimental results and the modified models for various overload angles.

β	Front Side					Back Side				
	Exp.	Model I		Model II		Exp.	Model I		Model II	
		Value	Error (%)	Value	Error (%)		Value	Error (%)	Value	Error (%)
0°	0.98	0.95	3.1	0.98	0	1.24	1.20	3.2	1.24	0
15°	0.73	0.75	2.7	0.78	6.8	1.02	1.03	0.9	1.07	4.9
45°	0.44	0.47	6.8	0.50	13.6	0.69	0.73	5.8	0.77	11.6
90°	0	0.02	100	0	0	0	0.02	100	0	0

Fig. 24 illustrates the mixed mode exponent estimated from experimental results and the modified models by considering welding residual stress.

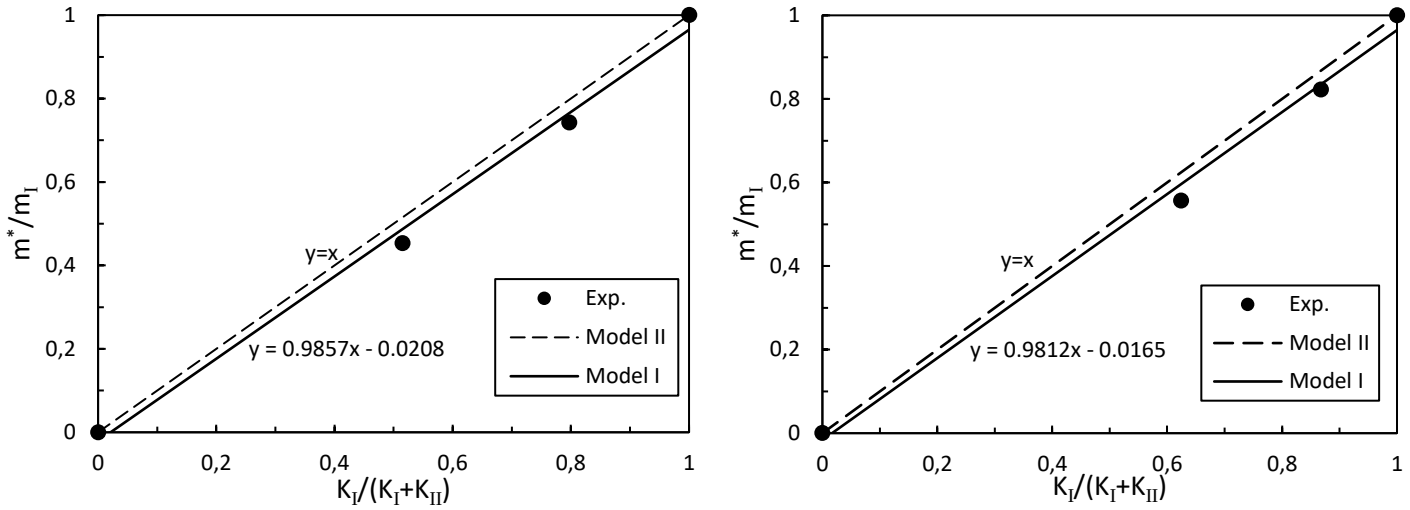

(a) (b)

Fig. 24. Normalized mixed mode exponent in terms of mode mixity including residual stress effect for (a) front side and (b) back side of the specimen.

As can be seen from Fig. 24, by adding the effect of residual stress into the previous models which were proposed based on non-welded specimens, mixed mode exponent can be predicted with high accuracy.

7. Conclusions

In the present paper, several experiments have been conducted to study the effect of the loading and overloading angle on fatigue crack growth of Al5083-H111. According to the obtained results, the following conclusions can be drawn:

- It was observed that in mixed mode experiments the FCGR in welded joint is lower than that in base metal which is due to compressive residual stress perpendicular to the initial crack plane. Also, the FCGR of the front and back side of specimen in each loading angle gradually became closer to each other and then they became equal. This is due to releasing residual stress. By increasing mode mixity the effect of the residual stress on the FCGR decreased rapidly, since the crack grows far from the weld zone.
- Plotting FCGR in terms of the effective stress intensity factor range (ΔK_{eff}), a more proper correlation was obtained between the FCGR data of welded joints with base metal in each loading angle.

- It was observed that the post weld heat treatment decreases retardation of crack growth since the compressive residual stress at the crack tip is released by heat treatment.
- According to the results of mixed mode overload experiments, pure mode I overload created the largest retardation. The amount of retardation decreased as the portion of mode II in the overload increased. No significant retardation was observed in specimen subjected to pure mode II overload.
- It was shown that the available models for non-welded specimens can not accurately predict the mixed mode exponent in case of welded joints. These models were modified by adding the effect of residual stress into them in such a way that the mixed mode exponent can be estimated with high accuracy.

Declaration of interests

The authors declare that they have no known competing financial interests or personal relationships that could have appeared to influence the work reported in this paper.

Funding

This research did not receive any specific grant from funding agencies in the public, commercial, or not-for-profit sectors.

References

[1] Wilcox DV, Adkins H, Dickerson PB, Hasemeyer EA, Lockwood L. Welding aluminum. 6th ed. Florida: American Welding Society; 1972.

[2] Kim IT. Weld root crack propagation under mixed mode I and III cyclic loading. Eng Fract Mech 2005;72:523-34.

[3] Zhu ML, Wang DQ, Xuan FZ, Tu ST. In-situ observation of mixed mode fatigue crack growth behavior in heat affected zone of a welded joint. 13th International Conference on Fracture. June 16-21, 2013, Beijing, China.

[4] Tang L, Qian C, Li H. Mixed mode notch-crack fatigue propagation in the welding zone of 06Cr19Ni10 austenitic stainless steel: Effect of strain strengthening. Int J Mater Res 2016;107(8):747-51.

[5] Jie ZY, Li YD, Wei X. A study of fatigue crack growth from artificial corrosion pits at welded joints under complex stress fields. Fatigue Fract Eng Mater Struct 2017;40(9):1364-77.

[6] Ma S, Zhang XB, Recho N, Li J. The mixed-mode investigation of the fatigue crack in CTS metallic specimen. Int J Fatigue 2006;28:1780-90.

[7] Wang Q, Liu X, Wang W, Yang C, Xiong X, Fang H. Mixed mode fatigue crack growth behavior of Ni-Cr-Mo-V high strength steel weldments. Int J Fatigue 2017;102:79-91.

[8] Maljaars J, Pijpers R, Slot H. Load sequence effects in fatigue crack growth of thick-walled welded C-Mn steel members. Int J Fatigue 2015;79:10-24.

[9] Anderson TL. Fracture mechanics: fundamentals and applications. 4th ed. Florida: CRC Press; 2017.

[10] Paris PC, Tada H, Donald JK. Service load fatigue damage – a historical perspective. Int J Fatigue 1999;21:S35-46.

[11] Richard HA, Sander M. Fatigue crack growth: Detect - Assess - Avoid. Springer; 2016.

[12] Wheeler OE. Spectrum loading and crack growth. J Basic Eng 1972;94(1):181-6.

[13] Yuen BKC, Taheri F. Proposed modifications to the wheeler retardation model for multiple overloading fatigue life prediction. Int J Fatigue 2006;28:1803-19.

[14] Mehrzadi M, Taheri F. A material sensitive modified wheeler model for predicting the retardation in fatigue response of AM60B due to an overload. Int J Fatigue 2013;55:220-9.

[15] Lu YC, Yang FP, Chen T. Effect of single overload on fatigue crack growth in QSTE340TM steel and retardation model modification. Eng Fract Mech 2019;212:81-94.

[16] Shiraiwa T, Murakami T, Enoki M. Effect of overload on fatigue crack growth behavior of thin copper foil. Int J Fatigue 2019;126:202-9.

[17] Sander M, Richard HA. Finite element analysis of fatigue crack growth with interspersed mode I and mixed mode overloads. Int J Fatigue 2005;27:905-13.

[18] Sander M, Richard HA. Experimental and numerical investigations on the influence of the loading direction on the fatigue crack growth. Int J Fatigue 2006;28:583-91.

[19] Mohanty JR, Verma BB, Ray PK. Prediction of fatigue life with interspersed mode-I and mixed-mode (I and II) overloads by an exponential model: extensions and improvements. Eng Fract Mech 2009;76:454-68.

[20] Lee JM, Choi BH. Experimental observation and modeling of the retardation of fatigue crack propagation under the combination of mixed-mode single overload and constant amplitude loads. Int J Fatigue 2009;31:1848-57.

[21] Singh AK, Datta S, Chattopadhyay A, Phan N. Characterization of crack propagation behavior in Al-7075 under in-plane biaxial fatigue loading with shear overloads. Int J Fatigue 2020;134. https://doi.org/10.1016/j.ijfatigue.2020.105529

[22] Singh AK, Datta S, Chattopadhyay A, Phan N. Fatigue crack growth behavior in Al-7075 under in-plane biaxial loading with mixed-mode overloads. In: The Minerals, Metals & Materials Society (eds) TMS 2020 149th Annual Meeting & Exhibition Supplemental Proceedings. The Minerals, Metals & Materials Series, pp. 1465-78. Springer, Cham; 2020.

[23] Rege K, Grønsund J, Pavlou DG. Mixed-mode I and II fatigue crack growth retardation due to overload: An experimental study. Int J Fatigue 2019;129:105-227.

[24] Shahani AR, Shakeri I, Rans CD. Two engineering models for predicting the retardation of fatigue crack growth caused by mixed mode overload. Int J Fatigue 2020;132. DOI: 10.1016/j.ijfatigue.2019.105378

[25] Shahani AR, Shakeri I. Experimental evaluation of fatigue behavior of thin Al5456 welded joints. Fatigue Fract Eng Mater Struct 2020;43(5):965-77. DOI: 10.1111/ffe.13173

[26] Richard HA, Benitz K. A loading device for the creation of mixed mode in fracture mechanics. Int J Fract 1983;22(2):R55-8.

[27] Dassault Systèmes. Abaqus product documentation: Abaqus analysis user's manual, Version 6.14-2. Providence, RI, USA: Dassault Systèmes; 2014.

[28] Richard HA. Fracture mechanical predictions for cracks with superimposed normal and shear loading. VDI-Forschungsheft 631/85, Düsseldorf:VDI-Verlag; 1985 (in German).

[29] Richard HA, Linnig W, Henn K. Fatigue crack propagation under combined loading. Forensic Eng 1991;3:99-109.

[30] ASTM E647-15e1. Standard test method for measurement of fatigue crack growth rates. West Conshohocken, PA: ASTM International; 2015.

[31] Zentech International Limited. Zencrack user manual, Version 7.9-3. London: Zentech International Limited, 2015.

[32] Summers PT, Chen Y, Rippe CM, Allen B, Mouritz AP, Case SW, Lattimer Y. Overview of aluminum alloy mechanical properties during and after fires. Fire Sci Rev 2015;4:1-36.

[33] Moein H, Sattari-Far I. Different finite element techniques to predict welding residual stresses in aluminum alloy plates. J Mech Sci Technol 2014;28(2):679-89.

[34] Friedman E. Thermomechanical analysis of the welding process using the finite element method. ASME J Pressure Vessel Technol 1975;97(3):206-13.

[35] Fanous IFZ, Younan MYA, Wifi AS. 3-D finite element modeling of the welding process using element birth and element movement techniques. ASME J Pressure Vessel Technol 2003;125(2):144-50.

[36] Dehkordi YG, Anaraki AP, Shahani AR. Study of the effective parameters on welding residual stress relaxation in aluminum cylindrical shells under cyclic pressure. Thin Walled Struct 2019;143. DOI: 10.1016/j.tws.2019.106235

[37] Richard HA, Schramm B, Eberlein A, Kullmer G. Cracks under Mixed Mode loading: Questions and solutions for isotropic and graded materials. 13th International Conference on Fracture. June 16-21, 2013, Beijing, China.

[38] Dirik H, Yalçinkaya T. Crack path and life prediction under mixed mode cyclic variable amplitude loading through XFEM. Int J Fatigue 2018;114:34-50.

[39] Sheu BC, Song PS, Hwang S. Shaping exponent in wheeler model under a single overload. Eng Fract Mech 1995;51:135-43.